eChem
https://www.sciltp.com/journals/eChem

Review

Integrated Aqueous Electrochemical Energy Devices

Jie Li [1], Min Zheng [2], Yangjie Liu [3], Xinmei Du [1], Qian Sun [4,*], Yu Zhang [1,3,*] and Zhenhai Wen [3,*]

[1] College of Chemistry and Chemical Engineering, Xinyang Normal University, Xinyang 464000, China
[2] Department of Chemistry, National University of Singapore, 12 Science Drive 2, Singapore 117549, Singapore
[3] State Key Laboratory of Structural Chemistry, and Fujian Provincial Key Laboratory of Materials and Techniques toward Hydrogen Energy, Fujian Institute of Research on the Structure of Matter, Chinese Academy of Sciences, Fuzhou 350002, China
[4] Department of Mechanical & Industrial Engineering, University of Toronto, Toronto, ON M5S 3G8, Canada
* Correspondence: qian.sun@utoronto.ca (Q.S.); zhangyu@xynu.edu.cn (Y.Z.); wen@fjirsm.ac.cn (Z.W.)

How To Cite: Li, J.; Zheng, M.; Liu, Y.; et al. Integrated Aqueous Electrochemical Energy Devices. *eChem* **2026**, *2*(1), 7. https://doi.org/10.53941/echem.2026.100007

Received: 27 March 2026
Revised: 25 May 2026
Accepted: 4 June 2026
Published: 25 June 2026

Abstract: Integrated aqueous electrochemical energy devices (IAEEDs) are emerging as a transformative paradigm in sustainable energy technology, unifying energy generation, storage, and chemical conversion within a single aqueous platform. Unlike conventional electrochemical systems that operate as isolated units, IAEEDs couple an aqueous power source, such as a Zn-air battery (ZAB) or fuel cell, with an electrolytic conversion cell, enabling cyclic operation without external electricity. This integrated strategy fully exploits the inherent merits of aqueous electrolytes, including high safety, low cost, and fast ionic transport, while simultaneously enabling hydrogen production, biomass upgrading, CO_2 reduction, and energy storage in one multifunctional system. Recent advances have highlighted the remarkable versatility and promise of these devices for constructing compact, efficient, and sustainable electrochemical technologies. In this Review, the design principles, reaction-coupling strategies, and representative architectures of aqueous IAEEDs are systematically summarized, with particular emphasis on the mechanistic origins of their synergistic performance. Key challenges, including catalyst compatibility, kinetic mismatch, interfacial regulation, and scalable integration, are also critically discussed. Finally, future directions are outlined to guide the development of more efficient, multifunctional, and modular aqueous electrochemical systems.

Keywords: integrated devices; aqueous electrochemical systems; sustainable technologies; battery; electrolytic

1. Introduction

The escalating global energy crisis and the severe challenges posed by climate change urgently demand the development of sustainable, low-carbon energy conversion and storage technologies [1–3]. The excessive consumption of traditional fossil fuels has led to rapidly increasing greenhouse gas emissions, particularly carbon dioxide (CO_2), while the direct use of electricity for chemical fuel production is constrained by intermittency and instability, presenting bottlenecks in economic viability and continuous operation [4,5]. Under these circumstances, the development of efficient, robust, and low-cost fuel-synthesis systems has emerged as a critical strategy for advancing energy transition and achieving carbon neutrality. Conventional electrochemical fuel production processes typically rely on external grid power, the reliability of which depends not only on the stability of power transmission infrastructure but also on fluctuations in electricity pricing. In addition, such systems often suffer from low system integration, multiple energy-conversion steps, and limited overall efficiency, leading to increased energy losses and operational complexity [6–8]. In response, self-driven electrochemical systems aimed

at achieving energy autonomy have attracted significant attention. Their core objective is to enable continuous and decentralized fuel production through internally coupled energy harvesting, storage, and conversion processes, thereby minimizing or eliminating reliance on external power input and enhancing overall energy efficiency and system integration [9–12].

Among various configurations of self-driven systems, the dual-circuit architecture based on aqueous electrochemical energy modules has demonstrated unique advantages and emerged as an important research direction in this field [13–16]. This architecture directly couples an aqueous chemical power source (such as metal-air batteries or fuel cells) as the driving module (Circuit 1) with another aqueous electrochemical electrocatalytic upgrading unit (e.g., a hydrogen-evolving electrolyzer or a CO_2 reduction device) as the driven module (Circuit 2), forming a complete, closed, self-powered system. In this design, the chemical energy stored in the metal anode or fuel is firstly converted into electricity, which subsequently drives the target upgrading reactions (such as low-carbon and hydrogen fuel generation) in the driven module, thereby achieving directed and autonomous conversion from self-generated internal power to value-added chemical fuel energy. This approach not only eliminates dependence on intermittent renewable sources or the external power grids but also, through functional decoupling, enables independent optimization of each circuit [17–21], thereby significantly improving overall system efficiency and operational stability. Consequently, the dual-circuit configuration provides a modular and scalable platform for decentralized, reliable, and sustainable fuel production.

Although recent reviews have discussed self-powered and integrated electrochemical systems, including solar-driven water electrolysis, triboelectric- and mechanically driven electrochemical systems, hybrid water electrolysis using thermodynamically favorable anodic reactions [22–27], the boundaries between these related concepts and integrated aqueous electrochemical energy devices (IAEEDs) remain insufficiently clarified. These studies are typically organized by energy source, harvesting–storage integration, reaction pairing, or temporal decoupling. In contrast, this Review defines IAEEDs as self-sustained systems in which an aqueous electrochemical power module, serving as the driver circuit, supplies the electrical work required by a separate aqueous electrocatalytic upgrading module, serving as the driven circuit, without continuous external bias during operation. Typical driver modules include aqueous metal-based batteries and aqueous fuel cells, whereas representative driven modules include electrolyzers and electrosynthetic reactors for hydrogen evolution, carbon dioxide conversion, and other value-added upgrading reactions. This distinction is important because the key scientific problem in IAEEDs is not simply whether two electrochemical reactions can be coupled, but whether two aqueous electrochemical circuits can be dynamically matched at the device level. The driver circuit must provide sufficient voltage, current density, stability, and electrolyte compatibility to satisfy the thermodynamic and kinetic requirements of the driven circuit. Meanwhile, the driven circuit imposes a load whose polarization behavior, mass-transport limitation, interfacial kinetics, and product distribution can feed back into the operating state of the driver circuit. Therefore, the actual performance of IAEEDs is governed by dynamic current matching, electrolyte and membrane compatibility, interfacial charge transfer, system-level energy losses, and degradation cross-coupling, rather than by the activity of an isolated catalyst alone.

The conceptual advance of this Review is therefore intentionally narrower but more device-specific than previous broad reviews on self-powered or integrated electrochemical systems. Rather than treating all autonomous, hybrid, or externally assisted electrochemical platforms as one category, this Review establishes IAEEDs as a distinct aqueous dual-circuit framework that links energy generation and chemical upgrading through an internally powered driver–driven architecture. This framework enables more rigorous comparison of thermodynamic compatibility, kinetic coupling, catalyst and electrode requirements, electrolyte selection, system efficiency, and operational durability across previously fragmented reports. In this sense, the present Review does not simply relabel existing self-powered systems; instead, it provides a clearer device-level classification and a mechanistic basis for evaluating aqueous self-driven electrochemical platforms. Herein, we systematically review recent progress in IAEEDs based on the "energy-generating module–electrocatalytic upgrading module" dual-circuit framework. We first establish the conceptual and mechanistic framework of IAEEDs by examining device-level integration, electrolyte-mediated ion transport, reaction-coupling principles, dynamic source–load matching, and system-level performance metrics. We then discuss key electrode materials and integrated design strategies for both energy-generating driver modules and electrocatalytic driven modules, emphasizing that catalyst activity, selectivity, stability, interfacial charge transfer, mass transport, and electrolyte/membrane compatibility must be optimized under coupled operating conditions rather than in isolated half-cell configurations. Subsequently, we summarize representative applications in self-powered hydrogen production, CO_2 electroreduction, ammonia synthesis, H_2O_2 generation, and other value-added chemical transformations. Finally, we highlight critical challenges and future opportunities in dynamic current matching, full-device energy-loss analysis, coupled

degradation diagnostics, standardized benchmarking, product separation, stackable architectures, and scalable process engineering.

2. Fundamentals Framework of IAEEDs

Integrated aqueous electrochemical energy devices (IAEEDs) operate through the direct coupling of an energy-generating driver unit and an electrocatalytic upgrading unit within an aqueous electrochemical environment. Their performance is therefore governed not by either subunit alone, but by the coordinated interplay among device-level integration, electrolyte consideration, reaction coupling, and system-level performance evaluation. In this framework, the device architecture determines how internally generated power is delivered from the driver to the driven module; the electrolyte defines the ionic pathway and local reaction environment; reaction coupling dictates whether the voltage, current, kinetics, and mass transport of the two circuits can be dynamically matched; and performance metrics provide the basis for quantifying energy utilization, selectivity, stability, and degradation under integrated operation. Establishing these principles is essential for moving IAEEDs beyond simple self-powered demonstrations toward rationally designed, efficient, durable, and scalable electrochemical systems. These principles are discussed in detail in Sections 2.1–2.4.

2.1. Device-Level Integration Principles

The foundation of IAEEDs lies in device-level integration, whose core architecture consists of a driver cell and a driven cell (Figure 1a). The driver cell, acting as the system's energy source, is typically an aqueous battery (e.g., ZAB) or a fuel cell (e.g., direct hydrazine fuel cell). Its function is to directly convert chemical energy stored in the metal anode or fuel into electrical energy via discharge reactions. The driven cell, serving as the system's energy load, is an electrochemical cell performing the target synthesis reaction, such as an electrolyzer for water splitting to produce H_2/O_2, or a synthesis cell for producing value-added chemicals via CO_2 reduction or biomass upgrading. The two units are connected into a closed loop through electrical coupling mechanisms. The simplest form is direct coupling, where the driver cell's output directly powers the driven cell. More complex systems may employ series or parallel connections to match voltage or current requirements. The highest level of integration is embodied in the shared electrolyte configuration, where both units physically share the same electrolyte chamber, separated only by a selective membrane (e.g., anion exchange membrane). This design significantly reduces system internal resistance and volume but presents stringent challenges for material compatibility and membrane performance.

2.2. Electrolyte Considerations

As IAEEDs operate in liquid-phase self-driven electrochemical environments, the electrolyte is not merely an ion-conducting medium but a central component that couples the chemical, electrochemical, and transport processes of the entire system. In a dual-circuit architecture, the electrolyte determines the ionic conductivity and ohmic resistance of each subunit, while also regulating local pH, reactant solubility, interfacial electric fields, double-layer structure, catalyst reconstruction, membrane compatibility, and product crossover. Therefore, electrolyte design directly affects not only the voltage and current matching between the driving and driven cells, but also the selectivity, stability, and overall energy efficiency of the integrated device. Aqueous electrolytes used in IAEEDs can generally be classified into alkaline, acidic, and neutral/near-neutral systems (Figure 1b). Alkaline electrolytes (e.g., KOH solution) are widely used due to their high ionic conductivity and excellent kinetics for reactions like oxygen reduction/evolution, making them particularly suitable for coupling with metal-air batteries and most electrolysis reactions. Acidic electrolytes (e.g., H_2SO_4) offer high proton conductivity and are often used in fuel cell-driven systems based on proton exchange membranes. Neutral electrolytes show potential for reactions sensitive to local pH, such as CO_2 reduction, by suppressing the competing hydrogen evolution reaction.

2.3. Reaction Coupling Strategies

The efficient operation of IAEEDs relies on precise thermodynamic matching and kinetic synergy between the driver and driven cells. Thermodynamic matching is the prerequisite for spontaneous system operation, requiring that the actual output voltage of the driver cell exceeds the sum of the thermodynamic potential and practical overpotential required by the target reaction in the driven cell (Figure 1c). Therefore, the discharge voltage platform of the driver module must be carefully matched with the voltage demand of the driven reaction. For example, water splitting has a theoretical voltage of 1.23 V but typically requires a practical cell voltage of 1.6–2.0 V, while CO_2 reduction to multicarbon products usually demands even more stringent kinetic and mass-

transport conditions. These reactions are difficult to drive using a single Zn–air battery because its practical working voltage is generally below 1.4 V, despite a theoretical voltage of 1.65 V [28]. Similarly, although a direct hydrazine fuel cell has a theoretical voltage of 1.56 V [29], its practical working voltage is usually below 1.1 V, meaning that two or more cells connected in series are often required to power energy-demanding upgrading reactions. In contrast, less energy-intensive processes, such as biomass-derived molecule oxidation or small-molecule oxidation coupled with hydrogen evolution, can often be driven by a single Zn–air or hydrazine fuel cell because their practical voltage demand is typically below 1.0 V. However, thermodynamic voltage matching alone is insufficient to guarantee efficient integrated operation. In a coupled IAEED, the actual operating point is determined by the intersection between the polarization curve of the driver circuit and the load curve of the driven circuit. In other words, the current delivered by the driver cell and the current consumed by the driven cell must be identical at any given moment, while the corresponding operating voltage is self-adjusted by the coupled system. Therefore, the practical performance of IAEEDs is governed not only by the open-circuit voltage of the driver and the equilibrium potential of the driven reaction, but also by activation polarization, ohmic resistance, mass-transport limitation, membrane resistance, and interfacial charge-transfer kinetics in both circuits.

This dynamic current matching is particularly important under realistic operating conditions. During continuous operation, the polarization behavior of both circuits can evolve with time due to reactant depletion, product accumulation, gas-bubble coverage, catalyst reconstruction, electrolyte concentration changes, pH drift, membrane hydration/dehydration, and electrode flooding or drying. These processes can shift the source–load intersection and lead to current decay, voltage fluctuation, or selectivity changes. For example, carbonate formation in alkaline electrolytes may increase ionic resistance and block porous electrodes, while gas accumulation at the driven electrode can reduce the electrochemically active area and increase local mass-transfer resistance. Such effects do not simply reduce activity in one half-cell; they change the entire coupled operating state of the IAEED.

Transient behavior is another key mechanistic feature of coupled operation. At start-up or during sudden load changes, the driver and driven circuits do not immediately reach a steady-state operating point. Instead, double-layer charging, local ion redistribution, and interfacial concentration gradients generate time-dependent current and voltage responses. These transient processes may cause temporary voltage overshoot, current oscillation, or mismatched reaction rates between the two circuits. In product-selective reactions such as CO_2 reduction, nitrate reduction, or biomass upgrading, such transient current fluctuations can alter local pH, intermediate coverage, and adsorption configurations, thereby affecting product distribution. Therefore, evaluating IAEEDs only under steady-state current or voltage conditions may overlook important dynamic features that determine long-term selectivity and durability.

Interfacial charge transfer under coupled operation also requires special attention. In conventional externally powered electrolysis, the applied potential can be independently controlled to optimize the interfacial reaction environment. In IAEEDs, however, the electrode potential of the driven module is indirectly determined by the instantaneous output of the driver module. As a result, the interfacial electric field, double-layer structure, adsorbate coverage, and charge-transfer resistance at the driven electrode are coupled to the discharge behavior of the driver cell. Any increase in interfacial resistance at either side, such as sluggish oxygen reduction in a metal–air battery, slow hydrazine oxidation in a fuel cell, or poor CO_2 activation in the driven electrolyzer, can reduce the total current and shift the operating potential away from the optimal selectivity window. This explains why catalyst design in IAEEDs should not only target high intrinsic activity, but also stable interfacial kinetics within the voltage and current window supplied by the driver circuit.

Accordingly, reaction coupling strategies should be designed from a system-level perspective. First, the driver module should provide a discharge plateau that overlaps with the practical operating window of the driven reaction. Second, the polarization curves of the two circuits should be matched to maximize the stable operating current while avoiding excessive overpotential losses. Third, catalysts and electrodes should be optimized to reduce activation barriers and interfacial charge-transfer resistance on both the driver and driven sides. Fourth, electrolyte, membrane, and flow-field engineering should be used to minimize ohmic loss, suppress crossover, stabilize local pH, remove gas products, and maintain reactant supply. Finally, dynamic operation tests, including start-up, long-term discharge, load variation, and intermittent operation, should be incorporated to evaluate whether the coupled system can maintain stable current matching, product selectivity, and energy efficiency over time. Therefore, the key challenge in IAEED reaction coupling is not merely to identify a driver cell with a sufficiently high nominal voltage, but to construct a dynamically compatible electrochemical pair in which thermodynamics, kinetics, transport, and interfacial charge transfer remain balanced throughout operation. This mechanistic understanding provides a more rigorous basis for designing efficient, stable, and scalable aqueous driver–driven electrochemical systems.

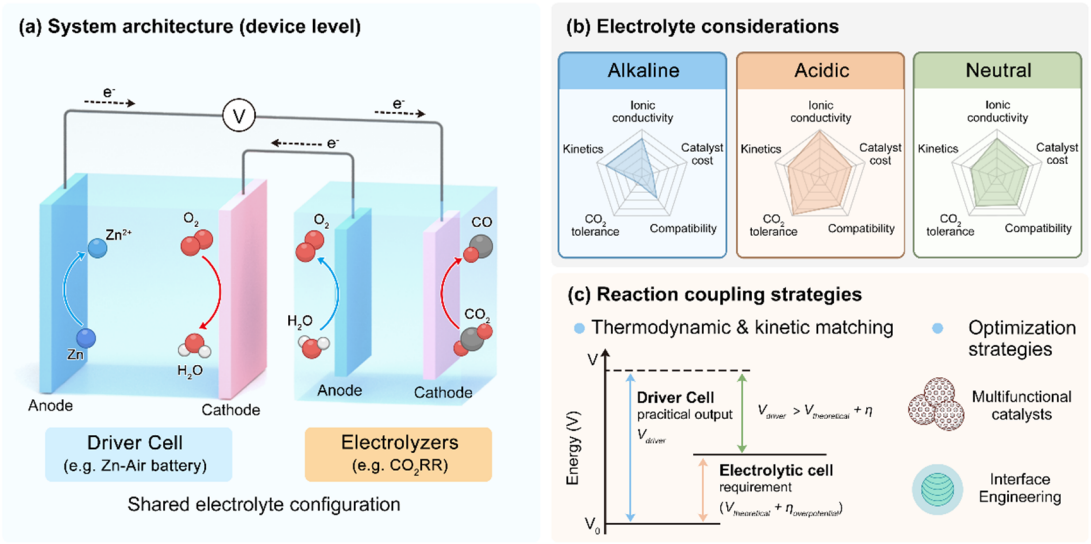

Figure 1. (**a**) Illustration of system architecture, (**b**) electrolyte considerations, (**c**) and reaction coupling strategies for self-powered integrated aqueous electrochemical energy devices.

2.4. Performance Metrics

A unified and comprehensive performance evaluation framework is essential for the objective comparison of different integrated systems. A unified and comprehensive evaluation framework is indispensable for the objective comparison and rational optimization of integrated systems. Evaluation criteria must capture not only individual electrochemical metrics but also system-level energy utilization and operational robustness.

Overall energy conversion efficiency represents a critical indicator of integrated system performance, but it should be evaluated by considering energy losses across the full driver–driven cascade rather than by the final product yield alone. In IAEEDs, the initial chemical energy stored in the driver module, such as metallic Zn or liquid fuel, is first converted into electrical output, then regulated and delivered to the upgrading module, and finally stored in target chemical products such as H_2, CO, formate, or other value-added chemicals. Energy losses can occur at each stage of this process, including activation and ohmic polarization in the driver cell, incomplete fuel utilization, self-discharge, contact and wiring resistance during electrical coupling, voltage/current mismatch between the two circuits, losses associated with voltage regulation or power adjustment units, overpotentials and parasitic reactions in the driven cell, membrane/electrolyte resistance, reactant crossover, mass-transport limitations, and product separation or collection losses. Practical operation should also consider whether the electrolyte can be continuously replenished, regenerated, or recycled without introducing additional energy penalties or composition drift. Therefore, the overall energy conversion efficiency should be rigorously defined, with clear system boundaries, as the ratio between the chemical energy stored in the final upgrading product and the initial chemical energy consumed by the driver module. This definition accounts for cumulative energy losses from primary chemical energy release to electricity generation, electrical transfer, target electrosynthesis, electrolyte management, and product recovery, thus providing a more holistic measure of real system effectiveness. Clear boundary definitions, consistent thermodynamic references, and loss-resolved reporting are essential for meaningful cross-study comparisons, because high Faradaic efficiency or high production rate may still correspond to low overall system efficiency if substantial losses occur during energy delivery, reaction coupling, electrolyte regeneration, or downstream product recovery.

FE and product selectivity remain central metrics for evaluating the upgrading module. However, in fully integrated systems, electron balance across the entire circuit must be carefully considered. The concept of overall Faradaic efficiency should incorporate potential parasitic reactions occurring in both the driving and driven units, thereby preventing overestimation of effective electron utilization. In addition, FE values should be reported together with the operating current density, applied or self-established voltage, electrolyte composition, membrane/separator type, reactant concentration or gas flow rate, product quantification method, and operation time. This is particularly important for reactions such as CO_2 reduction, nitrate reduction, ammonia synthesis, and H_2O_2 production, where product selectivity is highly sensitive to local pH, mass transport, crossover, and transient current fluctuations. Therefore, FE alone cannot fully represent integrated-system performance unless the testing conditions and system boundaries are clearly specified.

Power density, output capability, and product formation rate further characterize the practical applicability of IAEEDs. Areal power density, normalized to electrode geometric area, reflects device-level production capacity and facilitates comparison across reactor designs, whereas mass-normalized power density or activity provides information on catalyst utilization efficiency. However, cross-comparison among reported values remains challenging because power density may be normalized to different areas, including catalyst-coated area, membrane area, projected electrode area, or total device footprint. Similarly, H_2 production rates may be reported as mL min^{-1}, μmol h^{-1}, mmol h^{-1} cm^{-2}, L m^{-2} h^{-1}, or mass-normalized rates, making direct comparison difficult without conversion to a common basis. Therefore, future studies should report product formation rates using both absolute values and normalized values, preferably normalized to geometric electrode area, catalyst loading, and operating current, together with the corresponding Faradaic efficiency.

Operational stability is a decisive criterion for evaluating the technological viability of IAEEDs, but it should be analyzed in terms of degradation mechanisms rather than only operation time. Long-term tests, preferably exceeding 100 h under realistic integrated conditions, should report voltage/current retention, energy-efficiency evolution, FE variation, product-selectivity stability, electrolyte composition, and interfacial resistance. In IAEEDs, degradation may occur in the driver module, driven module, electrolyte/membrane, and interfacial architecture. Driver-side failure includes metal-anode corrosion, dendrite growth, fuel crossover, catalyst poisoning, air-cathode flooding, carbonate accumulation, and voltage decay. Driven-side degradation involves catalyst reconstruction, dissolution, surface poisoning, wettability loss, gas-bubble blockage, and changes in intermediate coverage, which can shift product selectivity and increase overpotential. Electrolyte and membrane degradation, including pH drift, carbonate formation, ion depletion, swelling, dehydration, and crossover, further increases ohmic resistance and reduces product purity. Importantly, these failure modes are coupled: degradation in one subunit can shift the polarization intersection between the driver and driven circuits, causing current mismatch, voltage fluctuation, and selectivity drift. Therefore, full-device stability evaluation should combine continuous operation with time-resolved polarization analysis, electrochemical impedance spectroscopy, electrolyte analysis, post-mortem characterization, and operando spectroscopy to identify the dominant degradation pathways under coupled operation.

Importantly, this comprehensive system-level evaluation represents a defining advantage of dual-circuit architectures. By intrinsically integrating energy generation with chemical upgrading, these architectures allow precise tracking of energy transfer and resource utilization throughout the entire process. This integrated perspective not only uncovers latent inefficiencies but also informs rational design strategies for system scale-up, techno-economic analysis, and practical implementation. As a result, system-level performance assessment offers a more accurate reflection of technological readiness and highlights the strategic potential of dual-circuit architectures for sustainable and decentralized fuel production.

3. Key Electrode Materials and Integrated Device Design

The performance of IAEEDs is governed not only by the intrinsic activity of electrode materials, but also by whether these materials can operate within the voltage, current, electrolyte, and mass-transport constraints imposed by the integrated driver–driven architecture. In conventional electrocatalysis studies, catalysts are commonly evaluated using half-cell metrics, such as overpotential, Tafel slope, Faradaic efficiency, and stability under externally controlled potential or current. However, in IAEEDs, the electrode potential of the driven unit is not independently imposed by a potentiostat. Instead, it is determined by the instantaneous output of the driving unit and the dynamic intersection between the polarization curves of the two coupled circuits. Therefore, catalyst design must be reconsidered from a device-level perspective.

For the driving cell, catalysts and electrode materials should provide a stable discharge voltage plateau, high power density, low internal resistance, and resistance to corrosion or passivation. For the driven cell, catalysts must deliver high selectivity and activity within the limited and sometimes fluctuating voltage/current window supplied by the driver. In addition, both circuits must be compatible with the same or separated electrolyte environments, membrane/separator chemistry, reactant supply, and product-removal pathways. These requirements make the catalyst design principles for IAEEDs fundamentally different from those for isolated electrocatalytic half-reactions.

Accordingly, this section discusses electrode materials beyond a conventional reaction-specific classification, instead emphasizing their functional roles in integrated device operation. From a device-level perspective, the key considerations include whether the driver electrode can sustain adequate voltage and current output during prolonged discharge, whether the driven catalyst can achieve high activity and selectivity within the voltage window supplied by the driver electrode, and whether both electrodes can retain structural and electrochemical

stability under dynamic operating conditions. These conditions include transient current fluctuations, local pH gradients, product crossover, electrolyte redistribution, and evolving interfacial microenvironments. In addition, rational interface and device engineering are required to minimize charge-transfer resistance and mass-transport limitations while maintaining architectural simplicity and operational robustness. Addressing the coupled challenges in materials design for driving and driven cells, together with interface/device engineering, is essential for translating catalyst-level advances into practically viable integrated aqueous electrochemical energy devices.

3.1. Materials for Energy-Generating Driving Cells

Driving electrodes determine the available voltage, current density, discharge stability, and power output of the integrated system (Figure 2a). Therefore, their relevance to IAEEDs should be evaluated not only by battery or fuel-cell performance alone, but also by whether their output can match the voltage and current demand of the driven upgrading reaction. A driver cell with high peak power but rapid voltage decay may be unsuitable for reactions requiring a stable potential window, such as CO_2 reduction or selective organic upgrading. Conversely, a driver with a moderate but stable discharge plateau may provide more reliable current matching for long-term operation.

Zinc-based aqueous batteries are widely employed as driver modules because Zn offers high theoretical capacity (820 mAh g^{-1}), low cost, and intrinsic safety [30]. Nevertheless, Zn dendrite formation, corrosion, parasitic hydrogen evolution, and electrolyte-induced passivation can shift the discharge voltage and increase internal resistance during operation. In an integrated device, these processes not only degrade the battery itself; they also alter the operating current delivered to the driven electrolyzer, thereby affecting product selectivity and energy efficiency. Therefore, strategies such as zincophilic carbon additives, conformal interfacial coatings, alloying, and electrolyte additives should be viewed as device-level stabilization approaches that help maintain source–load matching, rather than merely as battery-anode improvements [31–34].

At the air cathode of aqueous zinc–air batteries, ORR during discharge and OER during charge determine the voltage efficiency and durability of the driver module [35]. Bifunctional oxygen electrocatalysts, including transition-metal/nitrogen-doped carbons, perovskite oxides, spinel oxides, and heterostructured catalysts, have been widely developed to reduce ORR/OER overpotentials by tuning oxygen-intermediate adsorption and electronic structure [36]. For IAEEDs, however, the key requirement is not only low ORR/OER overpotential, but also stable discharge output under the operating current demanded by the driven unit. Air-cathode flooding, carbonate accumulation, catalyst oxidation, and gas-diffusion limitations can all increase polarization losses and destabilize the coupled system. Thus, air-electrode catalysts should be designed together with hydrophobic gas-diffusion layers, electrolyte management, and porous transport architectures to sustain stable oxygen transport and interfacial charge transfer. At the air cathode of aqueous zinc–air batteries, ORR during discharge and OER during charge determine the voltage efficiency and durability of the driver module [35]. Bifunctional oxygen electrocatalysts, including transition-metal/nitrogen-doped carbons, perovskite oxides, spinel oxides, and heterostructured catalysts, have been widely developed to reduce ORR/OER overpotentials by tuning oxygen-intermediate adsorption and electronic structure [36]. For IAEEDs, however, the key requirement is not only low ORR/OER overpotential, but also stable discharge output under the operating current demanded by the driven unit. Air-cathode flooding, carbonate accumulation, catalyst oxidation, and gas-diffusion limitations can all increase polarization losses and destabilize the coupled system. Thus, air-electrode catalysts should be designed together with hydrophobic gas-diffusion layers, electrolyte management, and porous transport architectures to sustain stable oxygen transport and interfacial charge transfer. For integrated systems that combine zinc–air chemistry with water splitting or other upgrading reactions, trifunctional catalysts capable of catalyzing ORR, OER, and HER are particularly attractive because they can simplify device configuration and reduce material complexity [37]. However, true trifunctionality in an IAEED requires more than high activity toward three reactions in separate tests. The catalyst must operate across different local pH, potential, and reactant environments while maintaining structural integrity and avoiding performance trade-offs between the driver and driven modes. Therefore, future trifunctional catalyst design should focus on dynamically adaptive active sites, robust electronic conductivity, and interface architectures that can sustain repeated changes in reaction environment during coupled operation [38].

Fuel cells represent another important class of driver modules. Hydrogen–oxygen fuel cells offer high energy-conversion efficiency, but their reliance on platinum-group-metal catalysts remains a major limitation [39]. In IAEEDs, fuel-cell catalysts should be evaluated according to both their intrinsic HOR/ORR activity and their ability to provide a stable voltage platform for the driven reaction. Precious-metal reduction, core–shell architectures, and M–N–C catalysts have shown promise for improving activity and durability [40,41]. Recent studies [42,43] have further emphasized the role of electronic structure modulation, interface engineering, and nanoscale morphology control in improving electrocatalytic performance. However, catalyst degradation, fuel

crossover, water management, and membrane resistance can change fuel-cell polarization behavior during operation, thereby influencing the driven cell. Therefore, catalyst stability under practical fuel utilization, humidity, and electrolyte/membrane conditions is central to integrated-device performance.

Direct liquid fuel cells, such as hydrazine fuel cells, provide attractive driver modules because liquid fuels offer high theoretical energy density and convenient storage [44]. Advanced HzOR catalysts, including Ru-based single-atom structures, metal alloys, phosphides, nitrides, and Ni/Co-based materials, have been developed to enhance hydrazine oxidation kinetics and poisoning resistance [45–47]. In the context of IAEEDs, the most important criterion is whether these catalysts can deliver a sufficiently stable voltage and current output to match the driven reaction without introducing crossover or safety issues. Thus, future driver-catalyst design should integrate activity, selectivity, poisoning tolerance, electrolyte compatibility, and fuel-management considerations into one device-level optimization framework.

3.2. Materials for Electrocatalytic Upgrading Driven Cells

Driven electrodes are responsible for converting internally generated electrical energy into target chemical products (Figure 2b). Unlike conventional externally powered electrolyzers, the potential of a driven electrode in an IAEED is constrained by the discharge behavior of the driver module. Therefore, driven catalysts should not only exhibit high activity and selectivity under ideal three-electrode conditions, but should also operate efficiently within the practical voltage/current window supplied by the driver. This requirement is especially important for reactions with narrow selectivity windows, such as CO_2 reduction, nitrate reduction, and selective biomass upgrading.

For HER, platinum-group metals remain benchmark catalysts in acidic media because of their near-optimal hydrogen adsorption energetics and rapid kinetics. However, their cost motivates the development of non-precious catalysts for alkaline and neutral systems. Transition-metal phosphides, sulfides, nitrides, carbides, and LDHs have been widely studied by optimizing hydrogen adsorption free energy, water dissociation ability, and interfacial charge transfer [48–57]. In IAEEDs, HER catalysts should also be assessed according to their compatibility with the driver output. A catalyst with excellent activity only at highly negative potentials may not be suitable if the driver cannot maintain that potential. Conversely, catalysts with moderate intrinsic activity but low charge-transfer resistance and broad operating tolerance may perform better in self-driven systems. Gas-bubble removal, wettability regulation, and electrode porosity are also critical because bubble accumulation increases local resistance and shifts the coupled operating point.

For CO_2 reduction, catalyst selectivity depends strongly on active-site identity, surface structure, oxidation state, electrolyte composition, and local microenvironment. Ag, Au, and M–N–C catalysts favor CO production, Sn and Bi-based catalysts favor formate, while Cu-based catalysts remain uniquely capable of producing multicarbon products through *CO adsorption and C–C coupling [58–66]. In an IAEED, however, CO_2RR catalysts must satisfy additional device-level constraints. First, the target product should be generated within the voltage window provided by the driver module. Second, the catalyst should tolerate current fluctuations and local pH changes caused by time-dependent driver discharge. Third, electrolyte and membrane selection should suppress carbonate formation, product crossover, and competing HER. These requirements mean that CO_2RR catalyst evaluation should include coupled-device tests, not only potentiostatic half-cell measurements.

Biomass-derived upgrading reactions, including glycerol, furfural, and HMF conversion, are particularly attractive for IAEEDs because many of these reactions require lower practical cell voltages than water oxidation and can be coupled with hydrogen evolution or other cathodic reactions [67–74]. In this case, the driven catalyst should be optimized not only for conversion and selectivity, but also for compatibility with the power profile of the driver cell. Ni-based catalysts that form NiOOH species under alkaline conditions are effective for HMF oxidation, while Cu- and Ag-based catalysts can promote selective hydrogenation pathways. However, organic substrates and intermediates may adsorb strongly, poison active sites, or change electrolyte composition during long-term operation. Thus, catalyst robustness against organic fouling, intermediate accumulation, and pH drift is essential for maintaining stable current matching in integrated devices.

Overall, the design of driven catalysts for IAEEDs should follow four device-oriented principles. First, the catalyst should operate in the voltage/current window provided by the driver module. Second, it should maintain product selectivity under dynamic rather than strictly fixed-potential operation. Third, it should be compatible with the electrolyte, membrane, and reactant/product environment of the integrated system. Fourth, it should minimize interfacial charge-transfer resistance and mass-transport limitations so that the coupled operating point remains stable over time.

3.3. Interface and Device Engineering

The performance of IAEEDs depends not only on the intrinsic activity of catalysts but also on how effectively catalyst layers, electrolytes, membranes, gas/liquid transport pathways, and electrical connections are integrated into a coupled driver–driven architecture. In contrast to conventional electrocatalytic systems, where the electrode potential can be externally controlled, IAEEDs operate under internally generated voltage and current. Therefore, interface and device engineering must address a broader set of requirements, including source–load matching, low internal resistance, efficient mass transport, suppressed crossover, product separation, and stable operation under dynamic current output.

At the interfacial level, the gas–liquid–solid triple-phase interface (Figure 2c) is particularly important for gas-involving reactions such as ORR in metal–air batteries, HER, CO_2 reduction, and fuel-cell reactions. This interface governs not only reactant accessibility and product removal, but also local pH, ion distribution, charge-transfer resistance, and intermediate coverage. Hierarchical porous electrodes, catalyst nanoarrays, gas-diffusion electrodes, carbon cloth, metal foams, and nickel foam substrates have been widely used to enlarge electrochemically active surface area and facilitate electron/ion transport [75]. Their main advantage lies in enhancing mass transport and reducing concentration polarization, which is critical for sustaining high current density in both driver and driven units. However, these architectures also introduce practical trade-offs. Highly porous electrodes may improve activity but can suffer from flooding, gas blockage, electrolyte evaporation, mechanical fragility, or uneven current distribution during long-term operation. Therefore, the optimal interface is not necessarily the one with the highest surface area, but the one that maintains stable reactant delivery, product removal, and interfacial charge transfer under the coupled operating current of the integrated device. Membranes and separators are another central component in IAEEDs because they regulate ion transport, suppress reactant/product crossover, and maintain chemical separation between different reaction environments [76,77]. For integrated devices, this trade-off is more severe than in standalone electrolyzers because membrane resistance directly changes the polarization curve of the driven unit and therefore shifts the operating point of the whole driver–driven system.

At the device level, the coupling between the driver module and the driven upgrading module determines the actual operating voltage, current, product rate, and overall efficiency. The electrical output from the driver cell is directly delivered to the driven cell, and the working point of the integrated system is defined by the intersection between the polarization curve of the driver and the load curve of the driven reaction. This means that catalyst performance, electrode resistance, electrolyte conductivity, membrane resistance, and mass transport in either subunit can influence the entire system. For example, two Zn–air batteries connected in series are often required to provide a voltage above 1.8 V for overall water splitting [78], whereas a relatively stable-output direct hydrazine fuel cell may be more suitable for lower-voltage biomass oxidation or organic electrosynthesis [79]. Therefore, device configuration should be selected according to the voltage demand, current density, reaction selectivity window, and stability requirement of the target upgrading process.

Different electrical integration strategies offer distinct advantages and limitations. Direct coupling between the driver and driven units is structurally simple, minimizes power-conversion losses, and is attractive for proof-of-concept demonstrations. However, it provides limited control over the driven electrode potential and is vulnerable to current decay when the driver voltage decreases or the driven reaction resistance increases. Series connection of multiple driver cells increases the output voltage and enables more demanding reactions such as water splitting or multi-electron CO_2 reduction, but it also increases device complexity, internal resistance, and failure risk if individual cells become imbalanced. Parallel connection increases current output and supports larger electrode areas or higher production rates, but it requires careful current distribution to avoid local hot spots, unequal discharge, or nonuniform reaction rates. Hybrid series–parallel configurations offer more flexible voltage and current matching, but they demand more sophisticated device design and monitoring.

From a practical perspective, each interface/device strategy should be evaluated by its trade-off between activity, stability, efficiency, and complexity. Highly active catalysts or porous electrodes may improve short-term current density but may also accelerate flooding, crossover, or structural degradation. Membranes improve separation and selectivity but increase resistance and cost. Direct coupling simplifies the system but limits operating control. Additional power-management components can stabilize voltage/current output but reduce the simplicity and energy-autonomy advantage of IAEEDs. Therefore, the most promising device configurations are those that maintain stable polarization matching while minimizing auxiliary components and preserving high product selectivity.

Overall, interface and device engineering in IAEEDs should move from empirical assembly toward rational system-level design. Promising near-term directions include robust gas-diffusion interfaces with balanced

hydrophobicity/hydrophilicity, low-resistance membranes with strong crossover suppression, self-supported electrodes with stable mechanical and electrical contact, and modular series–parallel architectures that can match the voltage/current requirements of different upgrading reactions. In contrast, strategies that rely only on maximizing catalyst surface area or using complex device architectures without addressing long-term resistance growth, crossover, and operating-point drift remain less mature. Future studies should therefore report not only catalyst activity but also full-device polarization curves, source–load matching behavior, product distribution, energy efficiency, and durability under continuous coupled operation.

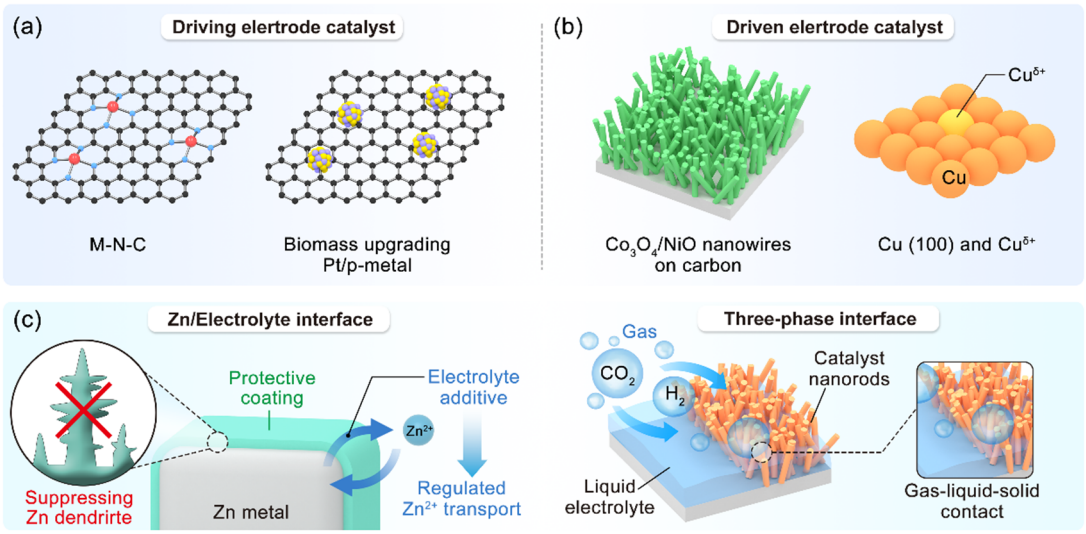

Figure 2. (**a**) Illustration of driving electrode catalyst. (**b**) Illustration of driven electrode catalyst. (**c**) Illustration of Zn/electrolyte interface and three-phase interface.yig.

4. Applications

Building on the fundamental principles and materials/device design strategies discussed above, this section summarizes representative applications of IAEEDs in sustainable fuel and chemical production. Rather than treating these examples as isolated self-powered demonstrations, we analyze them according to how the driver module, driven reaction, catalyst function, electrolyte environment, and device configuration are matched at the system level. In this context, hydrogen production represents the most mature application, benefiting from relatively well-established HER chemistry and the favorable voltage compatibility of Zn–air batteries, metal-based batteries, and fuel cells. CO_2 reduction provides a more demanding platform because product selectivity, local pH, mass transport, and multi-electron transfer must be controlled within the limited output window of the driver circuit. Emerging applications, including ammonia, hydrogen peroxide, and other value-added chemical production, further demonstrate the potential of IAEEDs to integrate energy generation, electrosynthesis, and waste valorization. Therefore, the following discussion highlights not only catalytic performance, but also device-level coupling, energy utilization, operational stability, and practical trade-offs across different application scenarios.

4.1. Hydrogen Production

Hydrogen production represents the most extensively explored and technologically mature application of IAEEDs, because the hydrogen evolution reaction can be coupled with a wide range of aqueous energy-generating modules and low-potential anodic reactions. In this section, we discuss three representative routes: Zn–air battery-powered water splitting, hydrogen production driven by other metal-based batteries with alternative anodic reactions, and fuel-cell-driven hydrogen generation. Across these systems, the central design principle is to match the voltage/current output of the driver module with the kinetic requirements of HER while minimizing the energy penalty associated with OER. Therefore, the following discussion emphasizes not only catalyst activity for HER/OER/ORR or alternative oxidation reactions, but also device-level coupling, energy efficiency, operational stability, and the practical trade-offs between system simplicity and reaction selectivity.

4.1.1. Water Splitting Powered by Zn-Air Battery

Due to the abundant oxygen supply from ambient air and the use of metallic zinc as an electron donor, ZABs exhibit exceptionally high theoretical energy densities. The theoretical gravimetric energy density of ZABs exceeds that of lithium-ion batteries by more than fivefold, while the volumetric energy density is approximately three times higher [80]. This intrinsic advantage arises from the fact that oxygen is supplied externally from the air rather than stored within the cell, significantly reducing the internal mass contribution of the cathode. Consequently, ZABs are considered highly promising power sources for the power source of the integrated electrochemical systems. In principle, their open-circuit voltage (1.65 V) [81] and practical discharge voltage (typically > 1.23 V) are sufficient to meet or exceed the thermodynamic requirement for water splitting, enabling direct coupling with electrolyzers. The performance of integrated ZAB, water splitting systems (Figure 3a) is governed by two key technical dimensions: the system-level energy coupling mechanism and the intrinsic activity of the electrocatalytic materials. At the device level, the working principle relies on the physical and electrical coupling of two electrochemical circuits through a series configuration. During discharge of the ZAB (Circuit 1), zinc oxidation at the anode ($Zn \rightarrow Zn^{2+} + 2e^-$) is coupled with the ORR ($O_2 + 2H_2O + 4e^- \rightarrow 4OH^-$) at the air cathode, generating a continuous electron flow. The resulting potential difference is directly applied to the water electrolyzer (Circuit 2) via an external circuit. Specifically, the positive terminal (air cathode) of the ZAB is connected to the anode of the electrolyzer, while the negative terminal (zinc anode) is connected to the cathode, forming a closed series circuit that enables spontaneous energy transfer. Within the electrolyzer, the supplied electrical energy drives the HER ($2H_2O + 2e^- \rightarrow H_2 + 2OH^-$) at the cathode and the OER ($4OH^- \rightarrow O_2 + 2H_2O + 4e^-$) at the anode.

The central challenge lies in developing a multifunctional material system capable of efficiently catalyzing all three core reactions of HER, OER, and ORR, simultaneously. The performance of these catalysts directly dictates the efficiency of both energy conversion stages: on the electrolysis side, HER and OER catalysts with low overpotentials significantly reduce the total cell voltage required for water splitting; on the battery side, highly active ORR catalysts enhance the discharge voltage and power output of ZABs. Consequently, current research is intensely focused on the rational design of multifunctional catalysts integrated within the self-driven upgrading system. This section systematically reviews these design strategies, which can be categorized into four primary directions (Table 1): (i) atomic and electronic structure modulation, (ii) interface and heterostructure engineering, (iii) construction of porous and hierarchical architectures, and (iv) integrated system and function-oriented design.

Atomic and electronic structure modulation. Precise control over the atomic coordination environment and electronic states of active sites is a foundational strategy for boosting the intrinsic activity of multifunctional catalysts.

Single-atom catalysts (SACs) represent the ultimate limit of atomic utilization. For instance, Co single atoms coordinated with various N species (pyridinic-N, pyrrolic-N, graphitic-N) in Co-NCS provide active sites for ORR, achieving a high half-wave potential [82]. Hybrid structures like Pt@CoN_4-G (Figure 3b, Top left), which feature atomically dispersed Pt and Co on N-doped graphene, exhibit strong metal-support interactions, leading to superior multifunctional activity [83]. Similarly, CoSA/N,S-HCS (Figure 3b, Top right), with Co atoms anchored on N,S co-doped hollow carbon spheres, benefits from synergistic cooperation between the Co-N_4 sites and electron-donating S dopants [38]. Further refinement of the coordination sphere, such as constructing an asymmetric Co-N_3P_1 configuration via P-doping (Figure 3b, Bottom left), can simultaneously optimize the adsorption of oxygen-containing intermediates for OER/ORR and hydrogen for HER [84]. Based on these SACs, the ZABs achieved large peak power densities and superior stability, making it possible to connect the water electrolysis device for high H_2 production rate of 450.1 L m^{-2} h^{-1} and nearly 100% of FE_{H2} under energy-generating current density of 100mA cm^{-2} (discharge process of ZAB).

Elemental doping offers a powerful means of engineering the electronic structure, thereby enhancing electrocatalytic activity and ultimately improving device performance in electrochemical systems. Based on the nature of the dopants, these strategies can be classified into three main categories: non-metal doping, metal-ion doping, and synergistic metal-nonmetal doping, each yielding distinct improvements in ZAB and electrolyzer metrics. Non-metal doping primarily involves heteroatoms like N, P, B, F, or S to modulate electronic structure and charge distribution in carbon matrices, offering a cost-effective route toward metal-free catalysts [85,86]. For instance, nitrogen, phosphorus, and fluorine tri-doped graphene has been shown to enable integrated device with high gas production rates of 0.496 for H_2 and 0.254 μL s^{-1} for O_2, respectively [85]. Metal-ion doping incorporates transition metal cations into host lattices to optimize electronic conductivity and stabilize active sites, leading to superior power output and durability [78,86–89]. For instance, doping Cr^{3+} into spinel $CoMn_2O_4$ yielded a high ZAB power density of 140.26 mW cm^{-2} and stable operation over 60 h, successfully driving a water-splitting

device [87]. Synergistic metal-nonmetal doping leverages the combined effects to create superior local chemical environments, often resulting in record-setting device performance [90–93]. Doping Cu, N, and S into porous carbon (Figure 3b, Bottom right) created a catalyst that achieved a remarkable ZAB peak power density of 197.9 mW cm^{-2} and outstanding stability over 250 h, subsequently driving water splitting at high production rates of 530 and 257 μmol h^{-1} for H_2 and O_2 [90].

Alloying provides synergistic interactions between different metal components, offering a powerful strategy to concurrently optimize the electronic structure and geometric architecture of electrocatalysts [94–98]. This dual optimization directly addresses the key limitations in integrated systems, leading to breakthrough performance in both power output (ZABs) and energy conversion efficiency (water electrolyzers). The core of this strategy lies in tailoring the d-band center and creating multifunctional interfaces. A prime example is the design of trimetallic PtCo/Ir fishbone-like nanowires (FBNWs), where the precise alloying ratio induces interfacial stress and a hetero-d-band-junction effect [94], resulting in a water electrolyzer that operates at a remarkably low voltage of 1.53 V (@10 mA cm^{-2}, acidic). This demonstrates how alloying can create a unified catalyst that drives the entire cycle with high efficiency. Beyond electronic effects, alloying is seamlessly integrated with multidimensional nanostructuring to enhance mass/charge transport. For instance, NiFe nanoalloys in situ coupled with a 3D N-doped carbon nanofiber network create a freestanding electrode [95], achieving high ZAB power density (140.1 mW cm^{-2}) and superior cycling stability (700 cycles), while the two liquid series-connected ZABs successfully powered a water electrolysis device with continuous O_2 and H_2 production at respective 1.78 and 3.57 μL s^{-1} over 6 h. Extending alloy engineering to systems with heteroatom-regulated electronic structures further expands the design landscape. A representative case is the integration of partially phosphatized FeCo bimetallic centers into a phosphorus and nitrogen co-doped carbon substrate (FeCo-P/PNC) [96], which results in a high peak power density of 195.1 mW cm^{-2} in aqueous ZABs and enables overall water-splitting system at a low operating voltage of 1.71 V, highlighting the effectiveness of combined alloying and heteroatom doping to simultaneously enhance driver and driven reactions in integrated systems. Advancing toward more complex multiphase alloy architectures further amplifies performance by exposing more active interfaces.

Pushing the boundaries of composition complexity, high-entropy alloys (HEAs) like FeNiCuWRu represent the pinnacle of this design philosophy [99]. The extreme cocktail effect and lattice distortion in HEAs create unique electronic structures and highly active, durable surfaces. This translates into unprecedented device-level performance, including an extraordinary ZAB peak power density of 537 mW cm^{-2} and exceptionally high-rate hydrogen production (2250 L m^{-2} h^{-1}), showcasing the ultimate potential of alloying engineering for integrated energy-output and fuel-generation devices.

Interface and heterostructure engineering. Constructing well-defined interfaces and heterostructures is crucial for facilitating charge transfer, integrating multiple functions, and stabilizing active components.

Catalysts featuring multi-interfacial compositions and multi-valent states often exhibit remarkable performance by optimizing electronic configurations and creating synergistic active sites. A prime example is the introduction of a small fraction of Ru^0 and RuO_x into dominant CeO_x to form a CeO_x(CO)/Ru^0(R^0)/RuO_x(RO) nanocomposite (NComp) [100], leading to superior trifunctional activity for ORR ($E_{1/2}$ of 0.936 V), OER (η_{10} of 166 mV), HER (η_{10} of 58 mV), an exceptional peak power density of 376.4 mW cm^{-2}, an ultra-low charge–discharge voltage gap of 0.247 V, and outstanding stability over 2000 h (12,000 cycles). Furthermore, two such ZABs connected in series efficiently powered a symmetric water electrolyzer, driving overall water splitting at just 1.49 V (10 mA cm^{-2}) and producing H_2 and O_2 at high rates of 399.3 and 199.6 μL min^{-1}, respectively, with corresponding FE of 98.9% and 98.4%. Similarly, interface engineering in core–shell structures are highly effective. A novel Ru/FeRu hybrid encapsulated in a carbon shell on N-doped carbon (Ru-FeRu@C/NC) was constructed, where the interfacial electronic interaction between Ru and FeRu regulates the electron configuration [101]. This catalyst achieved ultralow overpotentials of 23 mV for HER and 345 mV for OER at 10 mA cm^{-2}, alongside a high ORR half-wave potential of 0.90 V, confirming its excellent trifunctional capability as a robust catalyst.

Extending the design to heterostructured sulfides and hybrid phosphides further demonstrates versatility. For instance, NiS_2/CoS_2–O nanowires (NWs) with abundant oxygen vacancies and an interface-rich porous structure (Figure 3c, Top right) were designed [102], requiring only 235 mV to reach 10 mA cm^{-2} for OER. The assembled ZAB based on these NWs showed a high open-circuit voltage (OCV) of 1.49 V maintained over 30 h, and two series-connected ZABs could efficiently power a water-splitting device. Heterostructural design also includes combining different compounds to create synergistic interfaces and modulate electronic structures [103–105]. For example, hybrid nanoparticles like FeCo/Co_2P embedded in N,P-codoped carbon nanofibers (FeCo/Co_2P@NPCF, Figure 3c, Bottom left) demonstrate a remarkable synergy, where FeCo nanoparticles primarily contribute to ORR activity while the Co_2P-FeCo interface enhances OER and HER, achieving a low bifunctional oxygen electrode

activity parameter (ΔE) of 0.77 V [103]. The assembled ZAB exhibits a high power density of 154 mW cm^{-2} and a charge-discharge voltage gap of 0.83 V at 10 mA cm^{-2}, while the driven overall water-splitting cell operates at 1.68 V to reach 10 mA cm^{-2}. Similarly, confining Co/MoC nanoparticles within N-doped carbon nanoboxes (Co/MoC@NC, Figure 3c, Top left) creates an interface that synergistically facilitates charge transfer [104], which enables a ZAB with a large peak power density of 221 mW cm^{-2}, a high specific capacity of 728 mAh g^{-1}, and a low charge-discharge gap of 0.41 V. It also drives overall water splitting at a low cell voltage of 1.57 V. Mixed-phase engineering further enhances activity [106–108], as seen in NiCu-MoS_2 microflowers (Figure 3c, Bottom right) with abundant active sites from 1T/2H phase mixing, which exhibit excellent pH-universal HER activity [106]. The ZAB based on this catalyst achieves a remarkable peak power density of 283 mW cm^{-2} and the overall water-splitting cell operates at 1.622 V. Other prominent heterostructures include Co_3W_3C/CoP nanoparticles embedded in N,P-doped porous carbon fibers, which show low overpotentials for HER (139 mV) and OER (200 mV), a ZAB power density of 205.5 mW cm^{-2}, and an efficient water-splitting voltage of 1.49 V [107].

A sophisticated approach involves crafting homologous Mott-Schottky (MS) electrocatalysts through heterojunction integration [109]. The MS junction precisely modulates the electronic structure (e.g., d-band center), provides dual-electron transfer channels, and lowers energy barriers for intermediate reactions. ZABs equipped with these MS catalysts achieve high power density and record-breaking ultra-long cycle life in both aqueous and solid-state configurations, while also driving durable water splitting at low cell voltages, outperforming benchmark noble-metal catalysts.

Design of porous and hierarchical architectures. Engineering catalysts with porous and hierarchical structures maximizes the exposure of active sites, improves mass transport, and increases structural stability, all critical for high-current-density operation in integrated self-powered devices.

Zeolitic imidazolate framework (ZIF) derivatives are excellent precursors for constructing hierarchical catalysts due to their tunable compositions, well-defined porosity, and controllable morphologies. For instance, a ZIF-derived catalyst (CoFeN-NCNTs//CCM, Figure 3d, Top) exhibits a high power density of 145 mW cm^{-2}, a low voltage gap, and exceptional stability over 445 h [37]. Similarly, Co-MOF-derived O-doped carbon (Co-MOF-800) delivers a peak ZAB power density of 144 mW cm^{-2} and stable cycling for 510 cycles [110], while 2D Co quantum dots in N-doped carbon layers (Co@NCL) achieves a high power density of 170 mW cm^{-2} and efficient water splitting at 1.70 V [111]. In another approach, pyrolysis of bimetallic ZIFs on cellulose nanofibers ($FeZn_4$Co-ZIFs@CNFs) produces porous composites with well-dispersed active sites, enabling a ZAB power density of 107.6 mW cm^{-2} [112].

Beyond MOF derivatives, the versatility of hierarchical design extends to the rational construction of diverse and architecturally sophisticated nanostructures, enabling synergistic optimization of active-site exposure. Morphology control yields materials like donut-shaped CoP nanoparticles within a P,N co-doped carbon matrix (CoP@PNC-DoS), which shows a low ORR/OER potential gap of 0.781 V and powers a ZAB with a 138.57 mW cm^{-2} peak power density and 150-h stability [113]. Hierarchical CuCoNC nanowire arrays constructed on Cu foam enrich multiple active species, enabling a ZAB-driven water splitting device to achieve a high hydrogen production rate of 69 μL s^{-1} [114]. The hybrid electrodes composed of 1D CoS_2 nanowires and 2D MXene nanosheets (CoS_2@MXene) form a robust architecture, rendering it particularly suitable for quasi-solid-state devices [115].

Three-dimensional architectures further amplify performance by integrating conductive scaffolds with interconnected porosity. A carbon hybrid with a 3D nano-forest architecture (CoFe-N-CNTs/CNFs) integrates synapse-like structures for enhanced mass and charge transport [116]. 3D N-doped carbon sheets loaded with Co/CoFe nanoparticles (Co/CoFeNC@N-CNF) achieve an outstanding ZAB peak power density of 292 mW cm^{-2} [117], while 2D N-doped carbon superstructures decorated with Co single atoms or Co_2P nanoparticles (Co-NCS/Co_2P-NCS) exhibit a high power density of 219 mW cm^{-2} and a minimal voltage gap [82].

Further innovative hierarchical systems have been developed to integrate multiscale structural organization with electronic modulation, thereby achieving simultaneous optimization of catalytic activity [82,118–123]. A monolithic Co-NC membrane that incorporates integrated Co atoms and nanoclusters within an interconnected hierarchical carbon network achieves excellent trifunctional activity (ORR $E_{1/2}$ = 0.858 V, OER η_{10} = 229 mV, HER η_{10} = 36 mV) and powers a ZAB with 181.3 mW cm^{-2} and outstanding stability exceeding 1600 h [82]. The development of anion-regulated 3D NiFe hydroxysulfide monoliths ($Ni_{1.9}FeS_{1.09}(OH)_{4.6}$, Figure 3d, Bottom left) demonstrates how compositional modulation and hierarchical self-supported architectures can be synergistically integrated to achieve multifunctional electrocatalysis [118]. In addition, the vertically aligned ReS_2/NiFe-LDH heteronanosheets (Figure 3d, Bottom right) demonstrate efficient HER and cascade system integration [120], which further exemplify the structural versatility achievable through hierarchical engineering.

Integrated system and function-oriented design. Beyond intrinsic catalytic activity and structural optimization, advanced catalyst development must align with the operational demands of integrated systems. This

requires simplified device architecture, efficient energy utilization, and long-term stability under practical working conditions. Accordingly, function-oriented design, where a trifunctional material simultaneously fulfills HER, OER, and ORR requirements, has emerged as a central strategy for dual-circuit configurations coupling ZABs with water-splitting units.

High-performance trifunctional catalysts exemplify this integrated design philosophy [124–129]. For instance, Pt@CoS_2-N-doped rGO (Pt@CoS_2-NrGO) [124], with its flower-like morphology providing abundant Pt active sites and facilitating rapid ion/electron transfer, enables a ZAB power density of 114 mW cm^{-2} and 55 h stability. A broader range of recently developed materials further embodies this integrated multifunctional strategy. MOF-derived Co_2P embedded in multi-doped porous carbon [126] shows catalytic activities comparable or superior to RuO_2/Pt/C benchmarks, enabling efficient ZABs and water-splitting devices. Through dianion regulation, $Ni(S_{0.51}Se_{0.49})_2$ on N-doped carbon ($Ni(S_{0.51}Se_{0.49})_2$@NC, Figure 3e, Bottom left) [129] attains low HER overpotential of 111 mV, OER overpotential of 320 mV (both at 10 mA cm^{-2}), and ORR half-wave potential of 0.83 V, along with a ZAB open-circuit voltage of 1.46 V and stability over 1000 cycles. Similarly, an iron/cobalt-containing polypyrrole hydrogel-derived catalyst (PPy/FeTCPP/Co, Figure 3e, Top left) integrating Fe–N–C and Co–N–C species achieves efficient trifunctional catalysis, enabling ZABs powered water splitting at rates of 280 μmol h^{-1} H_2 and 140 μmol h^{-1} O_2 [129]. These examples underscore the feasibility of employing unified electrode materials for both energy generation and consumption processes within dual-circuit systems.

Structural engineering further enhances system compatibility [130–133]. Hollow structures, such as the NiCoOS hollow polyhedron derived from MOFs [130], provide abundant active surfaces and facilitate mass transfer, enabling stable H_2 production over 17 h in a ZAB-driven water-splitting system. Core-shell configurations enable functional decoupling and independent optimization of catalytic sites. Core-shell Fe-Co_2P@Fe-N-C [132] and NiFe@N-graphite (Figure 3e, Bottom right) [133] integrate HER/OER-active cores with OER/ORR-functional shells, resulting in ZAB open-circuit voltages of 1.44 V and 1.48 V, power densities of 81.3 and 85 mW cm^{-2}, and extended stability over 283 h and 40 h, respectively. The construction of integrated, freestanding electrodes represents another significant advancement toward device simplification. For instance, Co@NC-CNTs@NiFe-LDH grown directly on carbon cloth serves as a mechanically robust and conductive electrode for flexible ZABs and self-powered water splitting, contributing to 760 h durability [119]. The double-shelled hollow CoS_2@MoS_2@NiS_2 polyhedron integrates multifunctional active centers within a compact architructure that shortens mass transfer paths, exhibiting ZAB-driven water splitting with H_2/O_2 production rates of 1/0.5 mL min^{-1} [134]. The graphene-sandwiched heterojunction-embedded layered lattice (G-SHELL, Figure 3e, Top right) represents a pinnacle of interface and structure engineering, simultaneously addressing overpotential, activity, and stability issues, surpassing Pt/C + RuO_2 benchmarks with a power density of 275.8 mW cm^{-2} and stable operation over 250 cycles [80].

Collectively, these function-oriented strategies reflect a paradigm shift in catalyst design, from maximizing isolated reaction activity to engineering integrable, multifunctional electrode platforms capable of operating efficiently within practical dual-circuit systems. While ZABs have been extensively studied in this context, other metal–air batteries (e.g., Al/Mg/Fe-air) similarly offer promising self-driven energy sources, capable of directly powering electrocatalytic upgrading energy conversions. These alternative systems further expand the scope of autonomous, renewable-powered fuel and chemical production technologies.

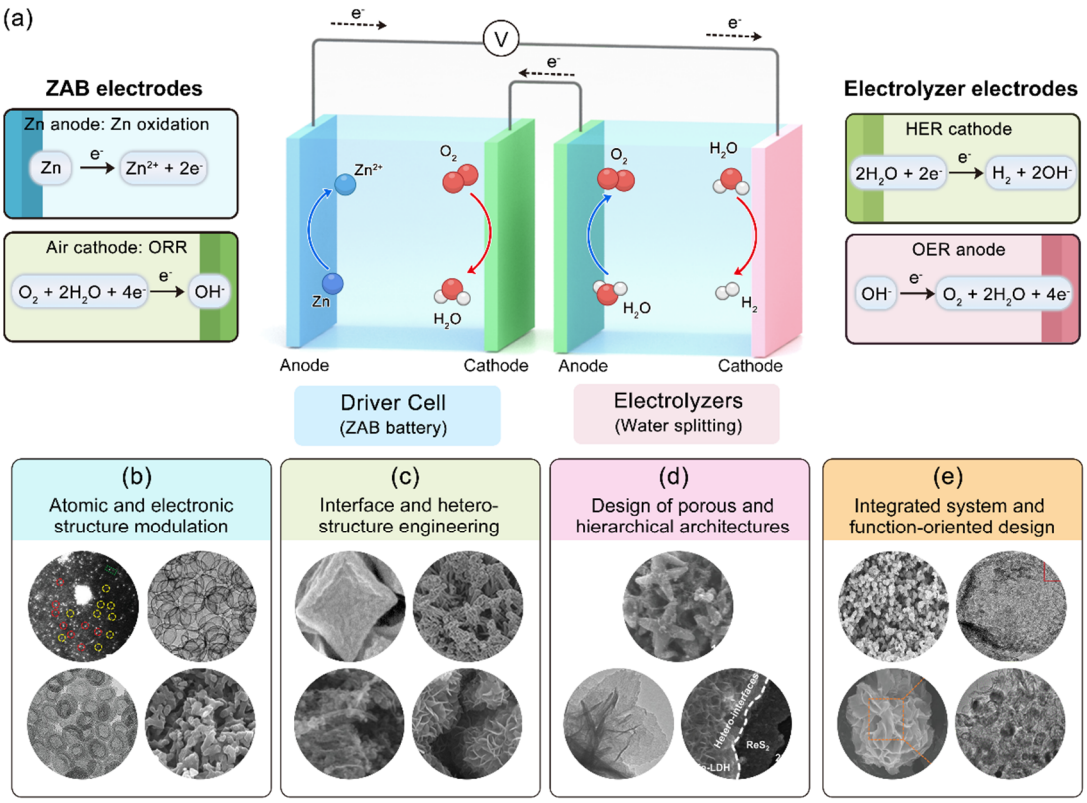

Figure 3. (**a**) Illustration of ZAB powered water splitting system. (**b**) *Top left*: Aberration-corrected HAADF-STEM image. Single Co atoms are marked by yellow circles, single Pt atoms are marked by red circles. Reproduced with permission. [83] Copyright 2023, John Wiley and Sons. *Top right*: TEM of CoSA/N,S-HCS. Reproduced with permission. [38] Copyright 2020, John Wiley and Sons. *Bottom left*: TEM of Co-N,P-HCS. Reproduced with permission. [84] Copyright 2022, John Wiley and Sons. *Bottom right*: SEM of Cu-N-SC-1100. Reproduced with permission. [90] Copyright 2021, American Chemical Society. (**c**) *Top left*: SEM of Co@IC/MoC@PC. Reproduced with permission. [104] Copyright 2021, American Chemical Society. *Top right*: SEM of NiS_2/CoS_2–O NWs. Reproduced with permission. [102] Copyright 2017, John Wiley and Sons. *Bottom left*: SEM image of $FeCo/Co_2P$@NPCF. Reproduced with permission. [103] Copyright 2020, John Wiley and Sons. *Bottom right*: FE-SEM NiCu–MoS_2. Reproduced with permission. [106] Copyright 2025, Royal Society of Chemistry. (**d**) *Top*: SEM of CoFeN-NCNTs//CCM. Reproduced with permission. [37] Copyright 2021, John Wiley and Sons. *Bottom left*: SEM of $Ni_{1.9}FeS_{1.09}(OH)_{4.6}$. Reproduced with permission. [118] Copyright 2018, John Wiley and Sons. *Bottom right*: FE-SEM image of the ReS_2/NiFe-LDH/CFP. Reproduced with permission. [120] Copyright 2021, American Chemical Society. (**e**) *Top left*: SEM image of the PPy/FeTCPP/Co. Reproduced with permission. [129] Copyright 2017, John Wiley and Sons. *Top right*: TEM of TEM image of G-SHELL. Reproduced with permission. [80] Copyright 2024, John Wiley and Sons. *Bottom left*: SEM of $Ni(S_{0.51}Se_{0.49})_2$@NC. Reproduced with permission. [128] Copyright 2022, John Wiley and Sons. *Bottom right*: SEM of $Fe_{0.5}Ni_{0.5}$@N-GR. Reproduced with permission. [133] Copyright 2018, John Wiley and Sons.

4.1.2. Hydrogen Production Powered by Other Batteries with Alternative Anodic Reactions

Beyond conventional metal-air batteries, a broader range of metal-based battery systems, including metal-H_2O/seawater batteries, Zn-Fe flow batteries, and metal-urea or metal-hydrazine batteries, has emerged as a promising platform for hydrogen production. These systems harness metal oxidation reactions, either coupled directly to hydrogen evolution or paired with alternative low-overpotential anodic reactions. Compared with conventional externally powered electrolyzers, such integrated configurations offer simplified device architectures, enhanced energy utilization efficiency, and the potential for off-grid or decentralized hydrogen generation.

Metal-H_2O batteries present a promising avenue for coupling energy storage with on-demand hydrogen production. The efficiency of such integrated systems hinges on the development of cathode that are highly active for the hydrogen evolution reaction limited metal oxidation reaction. A significant advancement in this area is the design of a Ru-based catalyst featuring coexisting Ru single atoms and clusters anchored on vacancy-rich α-MoC_{1-}

$_x$-coated carbon nanospheres (RuCS/SA/α-MoC_{1-x}/C). When employed as the cathode electrocatalyst, it enables both anion-exchange-membrane water electrolyzers and Zn-H_2O batteries (Figure 4a) to achieve outstanding performance, demonstrating its dual functionality and practical potential in hydrogen production systems [135], with 22.50 mW cm^{-2} peak power density (Figure 4b) and 760 mAh g^{-1} specific capacity (Figure 4c), outperforming the 20% Pt/C-based counterpart. Extending this concept to utilize abundant seawater resources, Xu et al. demonstrated a direct seawater electrolysis system driven by Mg-seawater batteries [136]. They developed a heterostructured MoNi/$NiMoO_4$ in Mg-seawater battery, which achieved a peak power density of 21.08 mW cm^{-2}, a continuous hydrogen evolution rate of 12.11 mL cm^{-2} h^{-1} and a high Mg-to-hydrogen conversion efficiency of 83.97%, showcasing a viable strategy for off-grid hydrogen production from seawater without relying on external power grids.

Redox-mediated flow battery systems further illustrate integrated design principles. A novel Zn−Fe flow battery (Figure 4d), featured by an Fe^{3+} reduction reaction (Fe^{3+}RR)-coupled zinc oxidation and an Fe^{2+} oxidation reaction (Fe^{2+}OR)-coupled HER, was established to power two series connected Fe^{2+}OR-coupled HER systems based on Fe^{2+}/Fe^{3+} cycling [137]. This battery exhibited 1.97 V OCV, and 100 h charge–discharge reversibility, and 65 mW cm^{-2} maximum power density. For practical applications, the Zn-Fe flow battery powered water-splitting electrolyzer (Pt-3@SXNS‖Pt-3@SXNS) only required 0.830 V to attain 20 mA cm^{-2}, much lower than that by Pt/C‖RuO_2 (1.804 V), 40 h stability at 20 mA cm^{-2}, and continuous H_2 production.

Hydrazine oxidation reaction (HzOR) provides a thermodynamically favorable anodic alternative. Lattice-confined Ru single atoms on octahedral Co_3O_4 (Ru–Co_3O_4) reduce the energy barrier for N_2H_2* intermediate formation and H* desorption, delivering excellent HzOR performance with −0.024 V vs RHE at 200 mA cm^{-2} and durability exceeding 200 h [138]. The hydrazine assisted Zn-redox cell driven hydrogen production system (Figure 4e), by decoupling and pairing HzOR with HER with Zn redox reservoir, demonstrated modular H_2 production with 0.48 kWh electricity per m^3 H_2 at 8.2 mL h^{-1}, with less electricity consumption than other anodic oxidation-HER coupling system (Figure 4f). When applied in a Zn-H_2 battery and an overall hydrazine splitting unit, an oxygen-functionalized $Ti_3C_2O_x$ MXene (Rh-SA/$Ti_3C_2O_x$) catalyst enables an ultra-high H_2 generation rate of 45.77 mmol h^{-1}, along with an open-circuit voltage of 1.27 V, a closed-circuit voltage of 0.75 V, and stable operation over 58 h [139].

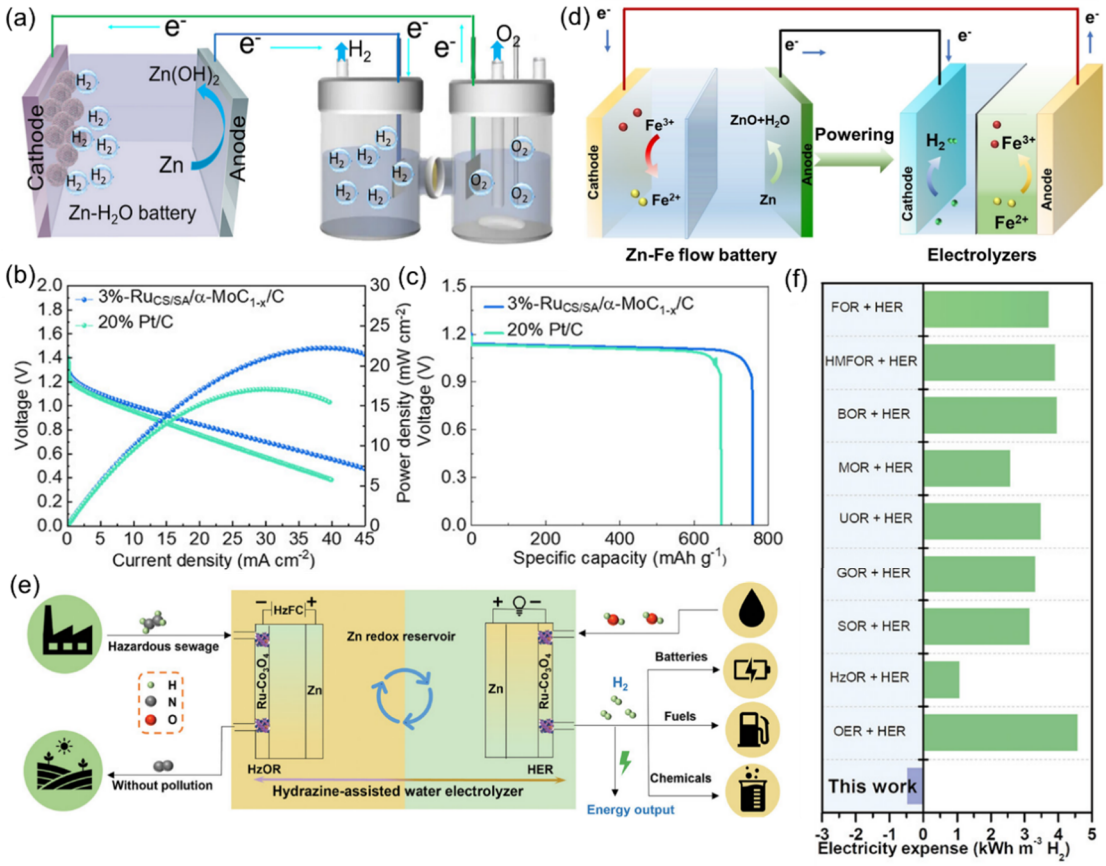

Figure 4. (**a**) Schematic illustration of the coupled configuration of double Zn-H_2O cells driving electrocatalytic water splitting. (**b**) LSV curves (left-hand y axis) and power density (right-hand y axis) of 3%-$Ru_{CS/SA}$/α-MoC_{1-x}/C

equipped Zn–H_2O cell. (**c**) plot of voltage versus specific capacity of 3%-$Ru_{CS/SA}$/α-MoC_{1-x}/C and 20% Pt/C. Reproduced with permission. [135] Copyright 2025, John Wiley and Sons. (**d**) Schematic illustration of a coupled configuration of a Pt-3@SXNS-equipped Zn−Fe flow battery driving a water-splitting electrolyzer catalyzed by Pt-3@SXNS for both HER and Fe^{2+}OR. Reproduced with permission. [137] Copyright 2022, John Wiley and Sons. (**e**) Schematic illustration of the discharge/charge processes for the HWE. (**f**) Comparison of the HWE with various water electrolyzers coupling anodic reactions (the oxidation reaction of furfural, hydroxymethyl furfural, benzyl alcohol, methanol, urea, glucose, and sulfur, respectively signify FOR, HMFOR, BOR, MOR, UOR, GOR, and SOR) and HER. Reproduced with permission. [138] Copyright 2023, John Wiley and Sons.

4.1.3. Hydrogen Production Powered by Fuel Cells

Direct hydrazine fuel cell (DHzFC) or hydrogen peroxide (DHHPFCs) driven systems. Hydrazine-assisted hydrogen generation overcomes the high overpotential of the OER in traditional hydrogen production system, replacing it with thermodynamically more favorable small-molecule oxidation reactions has emerged as a key strategy for achieving efficient, low-energy hydrogen production. Among these, the HzOR is particularly promising due to its extremely low equilibrium potential (−0.33 V vs. RHE) and the added environmental benefit of purifying toxic hydrazine-containing wastewater. Recent research has evolved from developing high-performance bifunctional (HER/HzOR) catalysts to constructing complete hydrogen production systems. These systems are powered by direct hydrazine fuel cells, using either oxygen (DHzFCs) or hydrogen peroxide (DHHPFCs) as the oxidant, which seamlessly integrates advanced catalyst design with systems engineering.

The performance of Zn-hydrazine batteries relies on advanced bifunctional catalysts such as Ru nanoclusters and single atoms supported on α-MoC/N-doped carbon nanowires (α-MoC/N−C/RuNSA) [140], NiCoPt-10 alloy [141], and Al-doped Ni_2P nanoflowers (Al-Ni_2P/NF) [142]. These catalysts employ various electronic structure modulation strategies, including the introduction of Pt active sites and Al doping-induced electron redistribution, to optimize H^* adsorption/desorption and hydrazine dehydrogenation kinetics. Consequently, the Zn-hydrazine batteries assembled with these catalysts exhibit the high energy efficiency of nearly 96%. Ultimately, the integrated systems (Figure 5a,b) enable continuous hydrogen production while simultaneously converting toxic hydrazine into environmentally benign nitrogen, achieving synergy between energy conversion and environmental remediation. The HzOR-assisted water electrolyzer based on NiCoP/NF exhibits low cell voltages of 107 mV and 212 mV at 100 and 200 mA cm^{-2}, respectively, and maintains stable operation for 96 h at 200 mA cm^{-2} benefiting from strong interfacial coupling effects. The corresponding Zn-hydrazine battery demonstrates an energy efficiency exceeding 95%, stable cycling for 240 cycles (80 h) at 5 mA cm^{-2}, and nearly 100% selectivity for gas products (H_2 during discharge, N_2 during charge) [143].

The Ru nanoparticle/mesoporous N-doped carbon (Ru/MPNC) composite presented abundant exposed ultrafine Ru particles fused into N-doped carbon walls which were stabilized by the in situ formed robust Ru-N metal-support interaction [144], with tailored electronic property of Ru sites for reduced barrier, optimal H^* adsorption free energies and N_2H_4 intermediates dehydrogenation, thus promoting HER and HzOR activity. Ru/MPNC contributed to small cell voltage of only 0.149 V to attain 50 mA cm^{-2} in the two-electrode electrolyzer, which was powered by direct hydrazine-H_2O_2 fuel cell to achieve H_2 production at 0.893 mmol h^{-1} and a power density of 97.6 mW cm^{-2}, surpassing that of the system with Pt/C. On the other hand, the doping effects in P/Fe-$NiSe_2$ accelerate charge transfer and optimize reaction kinetics, resulting in overpotentials of −168 mV for HER and 200 mV for HzOR at 100 mA cm^{-2}. The overall hydrazine splitting device constructed with this catalyst can operate stably for 100 h at 100 mA cm^{-2} [145].

High-performance bifunctional catalysts are the cornerstone of low-voltage hydrazine-assisted electrolysis. For non-precious metal catalysts, heteroatom doping and interface engineering are effective strategies to enhance performance [146–148]. For instance, P, W co-doped Co_3N nanowire arrays optimize the kinetics of H* adsorption/desorption and hydrazine dehydrogenation, enabling an overall hydrazine splitting cell to achieve a record-low cell voltage of only 28 mV at 10 mA cm^{-2} [146]. By constructing a tri-phase heterojunction interface among FeP, $FeNi_2P$, and N, P co-doped carbon (Figure 5c), the catalyst FeNiP-NPHC successfully balances and optimizes trifunctional catalytic activity for ORR, HzOR, and HER, providing a core material for seawater hydrazine splitting systems (Figure 5d) [147]. Furthermore, high-entropy alloy/intermetallic compound heterostructures utilize their multi-active-center surfaces and $^*N_2H_x$ intermediate spillover to enable ampere-level hydrazine electrooxidation at potentials > 0.08 V. The assembled electrolyzer achieves an ultralow cell voltage of 0.87 V at 500 mA cm^{-2} with exceptional stability for 1000 h, demonstrating significant potential to replace OER [149]. A self-powered H_2 production system assisted by hydrazine oxidation can be powered by direct hydrazine fuel cell.

For precious metal and alloy catalysts, research focuses on improving atom utilization efficiency and creating synergistic effects through structural design [29,150–161]. The hybrid $CoPt_3$/CoPt nanoparticles supported on N-doped carbon with low Pt loading (5.90 wt%) modulates electron distribution via metal-carbon hybridization, achieving efficient multifunctional catalysis for HER, HzOR, and ORR. This catalyst enabled the construction of a hydrogen production system without external electrical input [150]. The Pt@NiFc-MOF Mott-Schottky heterojunction utilizes the built-in electric field at the interface to promote charge transfer, demonstrating exceptional performance for HzOR, HER, and overall hydrazine splitting at ampere-level current densities. It was used to construct a high-performance direct liquid fuel cell with a peak power density of 415.2 mW cm^{-2} [29]. By optimizing the d-band center through metal-support interaction, the Ir nanoparticles anchored on B, N-codoped porous carbon catalyst achieved very low overpotentials for both HER and HzOR. The system it drove attained a remarkable hydrogen production rate of 53.08 mol h^{-1} m^{-2} [152]. RuPd alloy exhibits HER/HzOR overpotentials of −15.3/−77.9 mV at 10 mA cm^{-2}, achieving the self power system with 108.0 mW cm^{-2} peak power density [159]. Interface-disordered Pt enables an HzFC-OHzS system with OCV of 1.128 V, peak power density of 69.7 mW cm^{-2}, and H_2 evolution rate of 1.08 mmol h^{-1} [160].

Beyond these novel catalyst systems, research on hydrazine-assisted hydrogen production has established a diverse library of high-performance catalytic materials and systems [147,162–171]. For example, a bifunctional catalyst based on a 3D nanoporous Ni–Co perselenide nanorod array ($Ni_xCo_{1-x}Se$) enabled a direct hydrazine fuel cell to achieve a power density of 13.3 mW cm^{-2} at 54.7 mA cm^{-2} and a hydrogen evolution rate of 180 μmol h^{-1} with 98% FE [162]. The NiCo@C/MXene/CF catalyst, with exposed Ni_3Co (100) facets, effectively promotes the rate-determining step of HzOR, requiring only 25 mV and 43 mV to reach 100 and 500 mA cm^{-2}, respectively, while also showing high HER activity (49 mV at 10 mA cm^{-2}). A DHzFC based on this catalyst could efficiently power a hybrid seawater electrolyzer for hydrogen production, achieving a peak power density of 53.5 mW cm^{-2} and a solar-driven H_2 evolution rate of 6.0 mol h^{-1} g_{cat}^{-1} [164]. Hierarchical porous nanosheet arrays with abundant Ni_3N-Co_3N heterointerfaces also showed similar performance enhancement, enabling a DHzFC-driven system with a 60.3 mW cm^{-2} peak power density and an H_2 production rate of 0.65 mmol h^{-1} [166]. Fe-doped CoS_2 shows Pt-like HER activity and an HzOR overpotential of 129 mV at 100 mA cm^{-2}, with DHzFC peak power density of 246 mW cm^{-2} [167]. In addition, interface-optimized catalysts like Ni-Co-P/NF requires only 37/54 mV for HER/HzOR at 10 mA cm^{-2} and enable a DHzFC-powered electrolyzer with an H_2 production rate of 19.6 mol h^{-1} m^{-2} [171]. The tri-phase heterojunction FeNiP-NPHC enables a DHzFC-powered system with 0.98 V OCV and 31 mW cm^{-2} peak power density [147]. These hydrazine-assisted processes have been successfully applied in DHzFC-driven hydrogen production systems, collectively advancing the technology towards higher efficiency, stability, and integration.

Other fuel cell driven systems. Collectively, these fuel-cell-driven systems demonstrate a paradigm shift from self-driven energy conversion toward multifunctional platforms that integrate electricity generation, hydrogen production, chemical upgrading, and environmental remediation. To overcome the toxicity, high cost, and product separation challenges associated with hydrazine-based systems, increasing attention has been directed toward alternative anodic fuels for hydrogen production. These efforts can be broadly categorized into three strategic directions: (i) electrochemically favorable small organic molecules, (ii) biomass-derived fuels for integrated valorization, and (iii) chemical energy recovery from wastewater streams.

First, the approach involves the utilization of low-potential organic oxidation reactions to reduce cell voltage while enabling simultaneous electricity generation and hydrogen production. For instance, leveraging the thermodynamically favorable formaldehyde oxidation reaction (FOR), a hybrid alkaline-acidic fuel cell based on a Ru-doped Cu catalyst has been developed [172]. This configuration enables concurrent power generation and bipolar hydrogen evolution (Figure 5e), demonstrating that coupling organic oxidation with HER can substantially reduce energy input compared to conventional water electrolysis.

Second, the development of true biomass-derived fuel cells for sustainable and integrated resource upgrading. Examples include a direct furfural fuel cell (DFFC) that powers an electrolyzer to convert the biomass derivative into formic acid while producing hydrogen. Specifically, a DFFC based on Cu/RuCu nanowires exhibited an open-circuit voltage of 0.969 V and a peak power density of 193 mW cm^{-2}. When coupled with the coupled hydrogen evolution–furfural oxidation reaction (HER-FOR) electrolyzer, the integrated system operated at a low cell voltage of 0.43 V (100 mA cm^{-2}), achieving simultaneous production of pure H_2 at a rate of 6 mmol h^{-1} m^{-2} and oxidation of furfural to formic acid [173]. Similarly, a direct glycerol fuel cell system based on a trifunctional PtZn-IMC@NC catalyst enables simultaneous hydrogen production and the highly selective synthesis of valuable formate. The hybrid acid/alkali direct glycerol fuel cell (AA-DGFC) using this catalyst delivered a high peak power density of 286.8 mW cm^{-2} and stable operation for 68 h. The corresponding hybrid acid/alkali glycerol-hydrogen electrolyzer (AA-GHEC) required only 0.47 V to reach 100 mA cm^{-2}, significantly lower than

conventional water electrolysis (~1.08 V), and achieved stable H_2 production at 1700 μmol h^{-1} cm^{-2} (100% selectivity) alongside formate production at 930 μmol h^{-1} cm^{-2} (over 70% selectivity) [174].

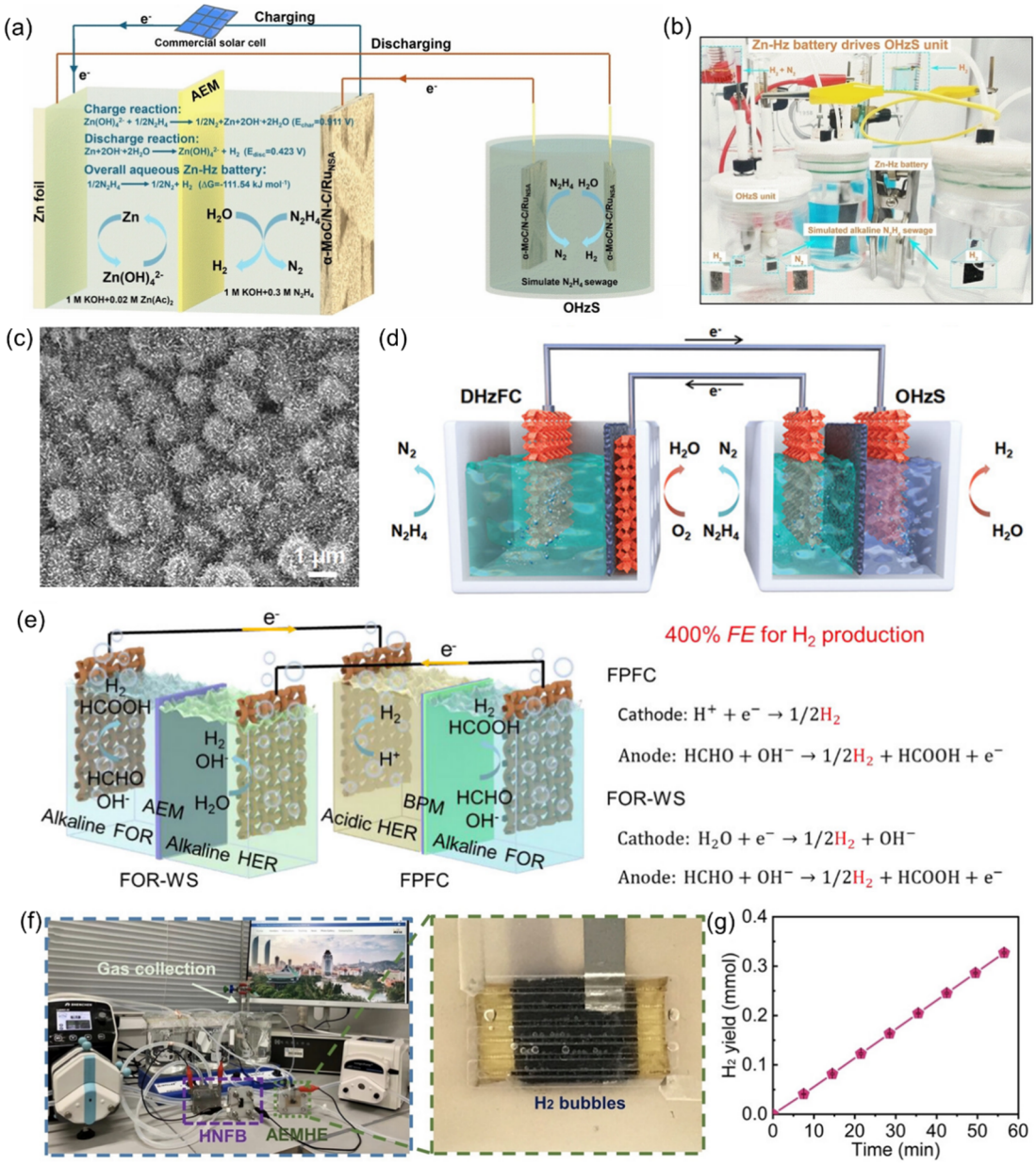

Figure 5. (**a**) Schematic illustration of the Zn−Hz battery-derived OHzS system. (**b**) Photo of the Zn−Hz battery-derived OHzS system with the N_2H_4 sewage as feed. Reproduced with permission. [140] Copyright 2024, John Wiley and Sons. (**c**) SEM images of FeNiP-NPHC. (**d**) Schematic drawing of DHzFC self-driven OHzS for sustainable hydrogen production and degradation of hydrazine degradation with the blue-green electrolyte region representing 1.0 M KOH + 0.5 M N_2H_4 seawater and the blue purple electrolyte region representing 1.0M KOH seawater. Reproduced with permission. [147] Copyright 2022, John Wiley and Sons. (**e**) Schematic illustration of an integrated system by connecting FPFC with FOR-WS to achieve 400% FE for H_2 production. Reproduced with permission. [172] Copyright 2026, John Wiley and Sons. (**f**) Digital photograph of the tandem HNFB and AEMHE devices for hydrogen production and (**g**) The hydrogen yield rate plot. Reproduced with permission [175]. Copyright 2023, John Wiley and Sons.

Third, innovative strategies have emerged to directly harvest chemical energy from wastewater streams, simultaneously achieving pollution control and fuel generation. The concept of a hydrazine-nitrate flow battery (HNFB) demonstrates simultaneous electricity generation, ammonia production, and subsequent hydrogen production from nitrogen-containing contaminants, providing a novel approach for pollution control and energy recovery. Specifically, a bimetallic RuCo precatalyst-based HNFB (Figure 5f) can deliver a peak power density of 12 mW cm^{-2} and operate continuously for over 20 h. Under a current density of 100 mA cm^{-2}, it achieves an

ammonia yield rate of approximately 0.35 mmol h^{-1} cm^{-2} (Figure 5g). The electricity generated by this process can further power a hydrazine electrolyzer to produce hydrogen fuel, thereby enabling a complete pathway for wastewater purification coupled with the generation of valuable fuels [175].

Building upon this, recent work has integrated a sulfide fuel cell with an electrolyzer to couple the treatment of sulfion (S^{2-})-containing industrial wastewater with hydrogen production. In this system, wastewater serves as the fuel for electricity generation, which then drives a sulfion oxidation reaction (SOR)-assisted electrolyzer for energy-saving hydrogen evolution, simultaneously yielding elemental sulfur and purified water. A key innovation lies in sourcing the required high-performance catalysts from spent lithium-ion batteries (LIBs). For instance, a bifunctional Co_9S_8 catalyst for SOR and the hydrogen evolution reaction (HER) is derived from spent $LiCoO_2$, while an Fe–N–P codoped carbon-based catalyst for the oxygen reduction reaction (ORR) is prepared from spent $LiFePO_4$. This design establishes a synergistic waste-treats-waste paradigm, transforming the chemical energy of toxic wastewater into electricity and hydrogen while enabling the high-value resource recovery of solid electronic waste. The reported system demonstrates an open-circuit voltage of 0.69 V, stable discharge for over 300 h, and a hydrogen production rate of 0.44 mL cm^{-2} min^{-1}, presenting a promising prototype for simultaneous environmental remediation, waste valorization, and decentralized clean energy production [176].

For hydrogen-production systems, the major energy losses generally originate from the discharge overpotential of the driver module, OER/HER overpotentials in the electrolyzer, ohmic resistance across membranes and electrolytes, gas-bubble accumulation, and voltage mismatch when multiple driver cells are connected in series. Therefore, future studies should report not only H_2 production rate and Faradaic efficiency, but also voltage efficiency, power-transfer efficiency, and long-term energy-efficiency retention under coupled operation.

Table 1. Summary of integrated systems for hydrogen production.

Driver Cell	Electrolyzer	Cathode	H_2 Production Rate	Power Density (mW cm^{-2})	Cycle Stability (h)	Stability (h)	Ref.
Solar cell (day) and ZAB (night)	water splitting	FeNiP@p-NPCF/CC	0.24 mL min^{-1}	117	500 cycles (500 h)		[177]
		silica-linked cobaloxime molecular	0.82 mmol h^{-1} (0.31 mL min^{-1}) 13.7% (STH)			12	[178]
A PSSP, two-series rechargeable ZABs		Co–NC@CC		170	725 h @ 5 mA cm^{-2}		[179]
Two ZAB in series		PPy/FeTCPP/Co	280 μmol h^{-1} (0.114 mL min^{-1})			12 h @ 10 mA cm^{-2}	[129]
Two tandem solid ZAB		CoSA/N,S-HCS	184 μmol h^{-1} (0.075 mL min^{-1})				[38]
seawater-based Zn–air batteries		Co-N-C		208.7			[84]
		$NiFe_2O_4$/IF				1600	[121]
		CoFeN-NCNTs//CCM		145		445	[37]
		CoFe-NiFe/NC	1.41 mL min^{-1}			27 h @ 50 mA cm^{-2} 15 h @ 100 mA cm^{-2}	[97]
		CoS_2@MoS_2@NiS_2	1 mL min^{-1}				[134]
		Cu-N-SC-1100	530 μmol h^{-1} (0.216 mL min^{-1})	197.9	250	15	[90]
		Co@NC-CNTs@NiFe-LDH		194	760 (liquid-type Zn-air battery, 10 mA cm^{-2})	120 (OWS, 20 mA cm^{-2})	[119]
ZAB powered water splitting		Co-doped Func CSCs-2M/α-MnO_2					[91]
		Pt/C	3.57 μL s^{-1} (0.214 mL min^{-1})				[95]
		$Ni_{0.5}Fe_{0.5}$@N-graphite	0.5 μL s^{-1} (0.03 mL min^{-1})				[133]
		G-SHELL	1.17 mmol h^{-1} (0.48 mL min^{-1})			41.6	[80]
		NiCu–MoS_2	0.43 mL min^{-1}			50	[106]
		Mo-$CuNCo_3$@CoN					[78]
		CoNC		181.3			[180]
		Co_3O_4@Ni_2P			177 (10 mA cm^{-2})		[105]
		GO-PANi-FP	0.496 μL s^{-1} (0.298 mL min^{-1})				[85]
		$FeZn_4Co$@CNFs					[112]
		CoP@PNC-DoS					[110]
		Fe doped MOF CoV@CoO				50	[123]

		Mo–$NiFe_2O_4$/IF					[88]
		$Ni(S_{0.51}Se_{0.49})_2$@NC				30	[128]
		Co@NCL				200	[111]
		Co-MOF-800				85	[110]
		N, B, and F triple-doped chain-like PCNFs	0.504 μL s^{-1} (0.0302 mL min^{-1})				[86]
		N, Co-CNTs				20	[93]
		$CO/R^0/RO$ NComp	399.3 μL min^{-1} (0.3993 mL min^{-1})				[100]
		$Ni_{1.9}FeS_{1.09}(OH)_{4.6}$					[118]
		CoS_2@MXene				20	[115]
		ReS_2/NiFe-LDH					[120]
		NF/CCO/FCH	6.25 μmol min^{-1} (0.153 mL min^{-1})				[181]
		Co_2P-NCS	0.204 mL min^{-1}			24	[82]
		$Co_{0.85}Se$/NC	STH (5.36%)	108	160 h @ 20 mA cm^{-2} with 40 min each cycle; 180 h @ 20 mA cm^{-2} with 4 h each cycle		[182]
		Ni–P/Fe–P	STH (4.6%)	138	1200 cycles (300 h)	35 h @ 10 mA cm^{-2}	[11]
		NiS_2/CoS_2–O NWs				60 min	[102]
		Ni_4Mo/MoO_2				50	[183]
		Co_3S_4/NF					[184]
ZAB	SOR-HER device	MoS_2/Ni_9S_8/NF	5.50 mmol min^{-1} $g_{catalyst}^{-1}$ (134.5 mL min^{-1} $g_{catalyst}^{-1}$)			5000 min	[185]

4.2. CO_2 Reduction

Zn-CO_2 battery has been deployed to self-drive CO_2-to-CO conversion (Figure 6a). A representative example involves the fabrication of coralloid gold catalysts that exhibited a high FE_{CO} of 94.2% at a current density of −60 mA cm^{-2}, with a CO production rate of 45.3 mL h^{-1} in a membrane electrode assembly (MEA) system. An aqueous Zn-CO_2 battery was constructed with a peak power density of 0.7 mW cm^{-2} and stable cycling for 68 h. This Zn-CO_2 battery was further integrated into a CO_2 electrolysis configuration, representing one of the earliest demonstrations of battery-driven autonomous CO_2 conversion. The coupled device achieved a maximum CO production rate of 0.44 mL h^{-1}, highlighting the feasibility of utilizing internal battery energy to drive CO_2 electroreduction without external electricity input [186].

Metal air batteries (MABs), featuring open-structured cathodes that eliminate the need for preloaded active materials, have emerged as promising next-generation energy storage technologies, due to their ultrahigh theoretical energy densities (Li-O_2: 5928 Wh kg^{-1}) [187], cost effectiveness, and environmental compatibility. In a representative rechargeable metal-air battery (Zn-air), Zn is oxidized to Zn^{2+} at the anode and oxygen reduction reaction (ORR) occurs at the cathode during discharge. While during charging, Zn^{2+} recoveries back to Zn, and oxygen revolution reaction (OER) happens at the cathode. Benefiting from their high theoretical energy density (1086 Wh kg^{-1}), low-cost, and intrinsic safety [188], rechargeable ZABs serve as efficient storage modules for intermittent renewable energy, further enabling electrolytic CO_2RR (Figure 6b).

Early demonstrations integrated two ZABs in series with a CO_2 flow cell, employing nitrogen-doped carbon-supported NiFe alloys (NiFe-NC) as bifunctional catalyst for CO_2RR and ORR [189]. This system delivered 95% FE_{CO} at 47 mA cm^{-2}, and maintained operation for 27 h with FE_{CO} gradually decreasing to 68.35%, probably due to ZnO deposition on the Zn anode which covers the Zn plate surface and suppresses reduction. Notably, NiFe–NC exhibited bifunctional catalytic activity, wherein Fe sites predominantly facilitated CO_2RR, while Ni sites enhanced ORR, achieving 91.6% FE_{CO} and 241.9 mA cm^{-2} in a flow cell, alongside a maximum ZAB power density of 185.92 mW cm^{-2}. This study provides a viable pathway toward large-scale CO_2 electroreduction powered by self-sustained metal–air batteries, eliminating the need for external electrical input.

Single-atom catalysts (SACs) have further advanced bifunctional electrocatalysis for CO_2 conversion. A Nb-N-C SAC with atomically dispersed Nb–N_4O sites achieved 90% FE_{CO} and an ORR half-wave potential ($E_{1/2}$) of 0.84 V (vs. RHE), together supporting a peak ZAB power density of 115.6 mW cm^{-2} [190] due to the maximum Nb atom utilization and the ordered mesoporous structure for efficient mass transfer. The Nb-N_4O sites in Nb-NC outperformed the graphitic-N sites in the NC with lower uphill energy barrier to *COOH formation, while the *O adsorbing on the Nb-N-C catalyst presented lower uphill energy barrier than that of NC, thus facilitating CO_2-to-CO conversion and ORR, respectively. The reduced energy barriers to the intermediate formation contribute to the potential-determining steps of CO_2RR and ORR. Two Nb-N-C-based ZABs in series assisted CO_2 conversion to CO with 3.75 μmol h^{-1} mg_{cat}^{-1} average productivity within 10 h, underscoring the promise of atomically engineered bifunctional catalysts.

Element doping strategy also plays a critical role in constructing multifunctional CO_2RR/ORR catalysts [191]. Fe-doped Sn nanoparticles immobilized on nitrogen-carbon (Fe–Sn/NC) exhibited over 100 h CO_2-to-CO conversion with 99% FE_{CO} at –0.47 V in an H-type cell, while the Fe–Sn/NC based Zn–CO_2 battery sustained over 99% FE_{CO} at 2-4 mA cm^{-2} discharge current densities and achieved 1.36 mW cm^{-2} peak power density. Because of the efficient ORR (0.88 V $E_{1/2}$) and ZAB performance (capacity: 752.5 mA h g_{zn}^{-1} at 10 mA cm^{-2} discharging current density, 160 h charging/discharging cycle test), the two series connected ZABs powered CO_2RR with strong catalytic stability (100 h), while the double Zn–CO_2 batteries with Fe–Sn/NC jointly produced CO at 1 μmol h^{-1} mg_{cat}^{-1} over 8 h and maintained 1.47 V voltage at both ends of the two batteries.

Nonmetal doping provides another avenue for enhancing bifunctional reactivity. Co-doping N and F into carbon nanotubes (NFCNT) induced charge redistribution, lowered the energy barriers of rate-determining steps ($CO_2 + H^+ + e^- \rightarrow {}^*COOH$, $O^* + H_2O \rightarrow OOH^* + H^+ + e^-$, $O_2 + H^+ + e^- \rightarrow OOH^*$) in CO_2RR, ORR, and OER, and increased the density of active paramagnetic centers [192]. Besides, NFCNT exhibited large surface area for abundant N, F doped species and active sites exposure, the abundant pyridinic-N and graphitic-N species promoted *COOH formation, whereas F doping modulated the electronic structure around N sites to generate additional active centers. Consequently, NFCNT-based ZABs achieved a high peak power density of 230 mW cm^{-2} and outperformed Pt/C + RuO_2 counterparts in durability (>100 cycles). When integrated into a CO_2RR configuration, two NFCNT-based ZABs connected in series with a CO_2 electrolyzer delivered 80% FE_{CO} and 60% total energy efficiency at −0.44 V vs RHE. N-Cnet exhibits high selectivity toward CO_2-to-CO production, achieving a FE_{CO} of up to 95% along with excellent long-term operational stability. Furthermore, its practical applicability was

demonstrated in electrochemical energy devices, including ZABs and microbial electrolysis cells. The ZAB assembled with N-Cnet delivered a maximum power density of 141 mW cm^{-2}, which shows the capability for the electrolysis configuration efficiently converted CO_2 into CO [193].

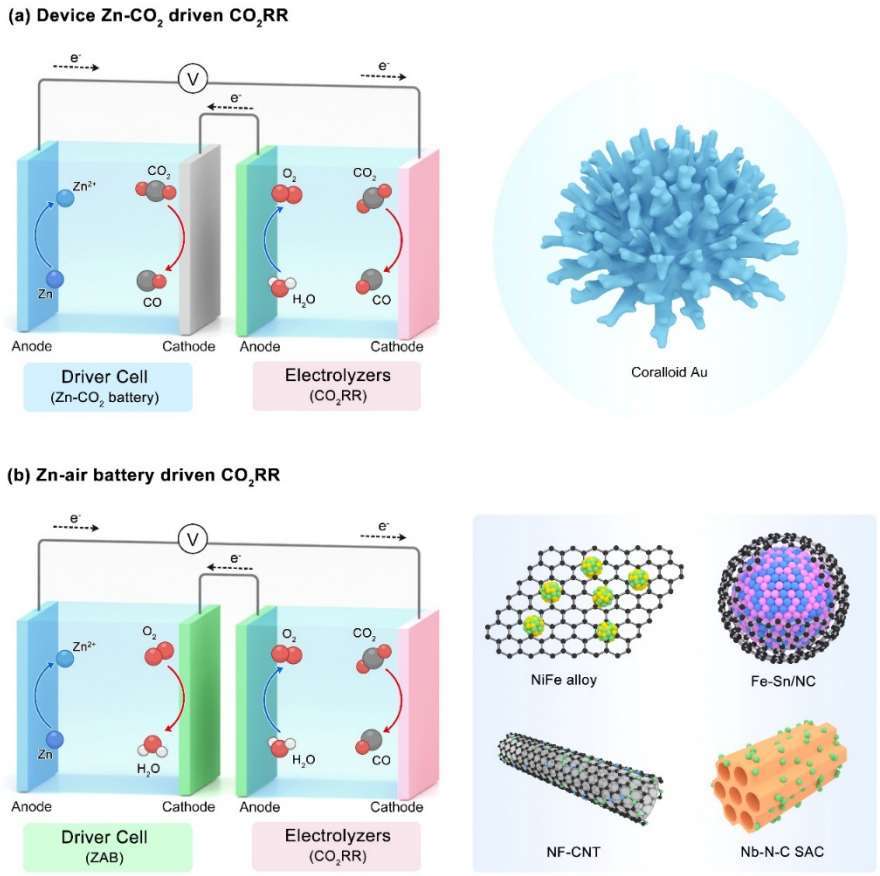

Figure 6. (**a**) Illustration of Zn-CO_2 battery driven CO_2RR. (**b**) Illustration of ZAB driven CO_2RR.

Compared with hydrogen production, self-driven CO_2 reduction involves additional energy-loss pathways associated with low single-pass CO_2 utilization, carbonate formation, product crossover, competitive HER, and downstream separation of dilute gas or liquid products. These losses should be explicitly considered when evaluating the practical efficiency of Zn–CO_2 or ZAB-driven CO_2RR systems.

4.3. Other Value-Added Chemical Production

Beyond hydrogen and CO_2-derived products, IAEEDs are increasingly being extended to the production of other value-added chemicals, where electrosynthesis can be coupled with waste conversion, pollutant removal, or resource recovery. This section focuses on two representative upgrading examples, ammonia and hydrogen peroxide, which highlight different aspects of integrated aqueous electrochemical design. Ammonia production demonstrates the potential of coupling nitrogen-containing waste streams, such as nitrate or nitrite, with thermodynamically favorable anodic reactions or battery-driven systems. Hydrogen peroxide production, in contrast, relies on selective two-electron oxygen reduction and benefits from integrated configurations that combine energy generation, oxidant utilization, and in situ environmental applications. These examples illustrate how IAEEDs can move beyond fuel production toward broader sustainable chemical manufacturing, while also introducing new challenges in selectivity control, product separation, electrolyte compatibility, and long-term stability.

4.3.1. Ammonia Production

The green synthesis of ammonia represents a major research focus, aiming to decarbonize this crucial chemical. Strategies have moved beyond the traditional nitrogen reduction reaction (NRR) coupled with water oxidation. Instead, systems are designed to couple NH_3 production from nitrate (NO_3^-RR) or nitrite (NO_2^-RR) with thermodynamically favorable anodic reactions to overcome low yields and high overpotentials, while achieving synergistic waste conversion. A prime example is the coupling of NO_x^-RR with the hydrazine oxidation

reaction (HzOR), where the design of catalytic atomic interfaces (e.g., Pd─O─Co) can accelerate hydrogen transfer kinetics in both reactions, enabling efficient NH_3 production alongside electricity generation in an integrated system (Figure 7a,b) [194].

Beyond direct light-driven approaches, battery-powered electrochemical systems demonstrate robust integration capabilities. ZABs are commonly employed as the core power source, and their performance relies on advanced trifunctional electrocatalysts, such as palladium single atoms [195] or amorphous Co_2B nanosheets [196]. These catalysts efficiently drive both the ORR/OER within the ZAB and the NRR/NO_3^-RR for NH_3 synthesis, enabling simultaneous electricity and ammonia generation in so-called ZAB-to-NH_3 systems. A similar integrated approach, utilizing a high-entropy alloy catalyst, allows a ZAB to drive NO_3^-RR for combined wastewater treatment and ammonia production (Figure 7c) [197]. Similarly, a Zn-NO_2^- battery powered system, employing a bifunctional Pd-$Co(OH)_2$ electrocatalyst, couples formaldehyde oxidation (FOR) with NO_2RR. This system achieves a remarkable ammonia production rate of ~44.69 mg h^{-1} cm^{-2} with a FE of ~96.36% and a significantly reduced energy consumption of 10.75 kWh kg^{-1} NH_3, enabling simultaneous NH_4Cl fertilizer production and formaldehyde degradation [198].

Building upon this concept of integrated chemical and energy conversion, recent research has further expanded toward systems capable of simultaneous multi-pollutant upgrading and resource recovery. One representative example employs a bifunctional Ru–Co_3O_4 heterostructured catalyst to synchronously trigger the NO_2RR and the ethylene glycol oxidation reaction (EGOR), thereby upgrading nitrite-rich wastewater and waste PET plastic into NH_3 and formic acid, a process powered by an integrated Zn-nitrite (Zn-NO_2^-) battery [199]. Another strategy makes use of dual-functional hierarchical Co_3O_4 nanostructures to couple NO_2^-RR with sulfion oxidation (SOR), producing ammonia while recovering elemental sulfur at a very low cell voltage; a proof-of-concept Zn-NO_2^- battery based on this catalyst is proposed to drive this cycle from wastewater to fertilizer and sulfur resources [200].

4.3.2. H_2O_2 Production

Hydrogen peroxide production offers a green alternative to the energy-intensive anthraquinone process. Shifting the perspective to hydrogen peroxide production, a conventional yet effective strategy involves coupling a ZAB with an electrolyzer dedicated to the two-electron oxygen reduction reaction ($2e^-$ ORR). Here, earth-abundant, metal-free carbon-based electrocatalysts (e.g., ordered mesoporous carbon) are engineered for high selectivity, performing the $4e^-$ ORR in the battery while favoring the $2e^-$ pathway in the electrolyzer, with H_2O_2 production at 323.9 mg/L for 2 h. The H_2O_2 produced can be immediately deployed for in situ degradation of wastewater pollutants, creating an integrated solution that combines energy storage with water purification [201].

A more innovative and integrated approach leverages biomass, specifically lignin, which serves both as a carbon-based catalyst precursor and as an electron donor (fuel). In this system, a direct lignin fuel cell provides the power for a paired electrolyzer (Figure 7d). The electrolyzer employs a B,O-doped carbonaceous catalyst, synthesized from lignin itself, to drive the two-electron oxygen reduction reaction ($2e^-$ ORR) using air as the oxygen source, achieving an exceptional H_2O_2 productivity of 11,812 mmol g^{-1} h^{-1} with a FE of 95.7% over 5 h (Figure 7e) [202]. This concept is further refined by employing the $[Fe(CN)_6]^{3-/4-}$ redox couple as an electron mediator for lignin oxidation on the fuel cell anode, effectively replacing the conventional oxygen evolution reaction. This substitution reduces the energy consumption of the coupled electrolyzer by 11.4%, elevates the total electron transfer efficiency of the entire system to 93.7%, and markedly improves its overall energy economy [202].

For ammonia, H_2O_2, and biomass-derived chemical production, the apparent reduction in electrolysis voltage should be balanced against product separation, electrolyte contamination, crossover, reactant utilization, and safety-related process costs. Therefore, the practical advantage of these systems should be evaluated using full-system energy efficiency rather than only cell voltage or Faradaic efficiency.

Across these applications, the maturity and practical relevance of IAEEDs vary substantially. Hydrogen production is currently the most mature direction because HER kinetics are well established, product separation is relatively straightforward, and the voltage requirement can be matched by ZABs, metal-based batteries, or fuel cells, especially when OER is replaced by lower-potential oxidation reactions. However, this direction still faces trade-offs between catalyst multifunctionality and long-term stability, as well as between direct coupling simplicity and controllable voltage/current output. CO_2 reduction offers higher carbon-utilization value but remains less mature because its product selectivity is highly sensitive to local pH, potential fluctuations, CO_2 availability, carbonate formation, and membrane crossover. Self-driven CO_2RR systems therefore require more stringent control of mass transport, electrolyte environment, and source–load matching than HER systems. Other value-added chemical production, including ammonia, hydrogen peroxide, and biomass-derived products, represents an

emerging opportunity because it can combine electrosynthesis with waste valorization or pollutant removal. Nevertheless, these systems should be critically assessed by considering reactant availability, product separation, electrolyte contamination, safety, and full-system energy efficiency. Overall, low-voltage hydrogen production coupled with waste or biomass oxidation appears closer to near-term translation, whereas self-driven CO_2-to-multicarbon conversion and ammonia synthesis remain less mature but scientifically important frontier directions.

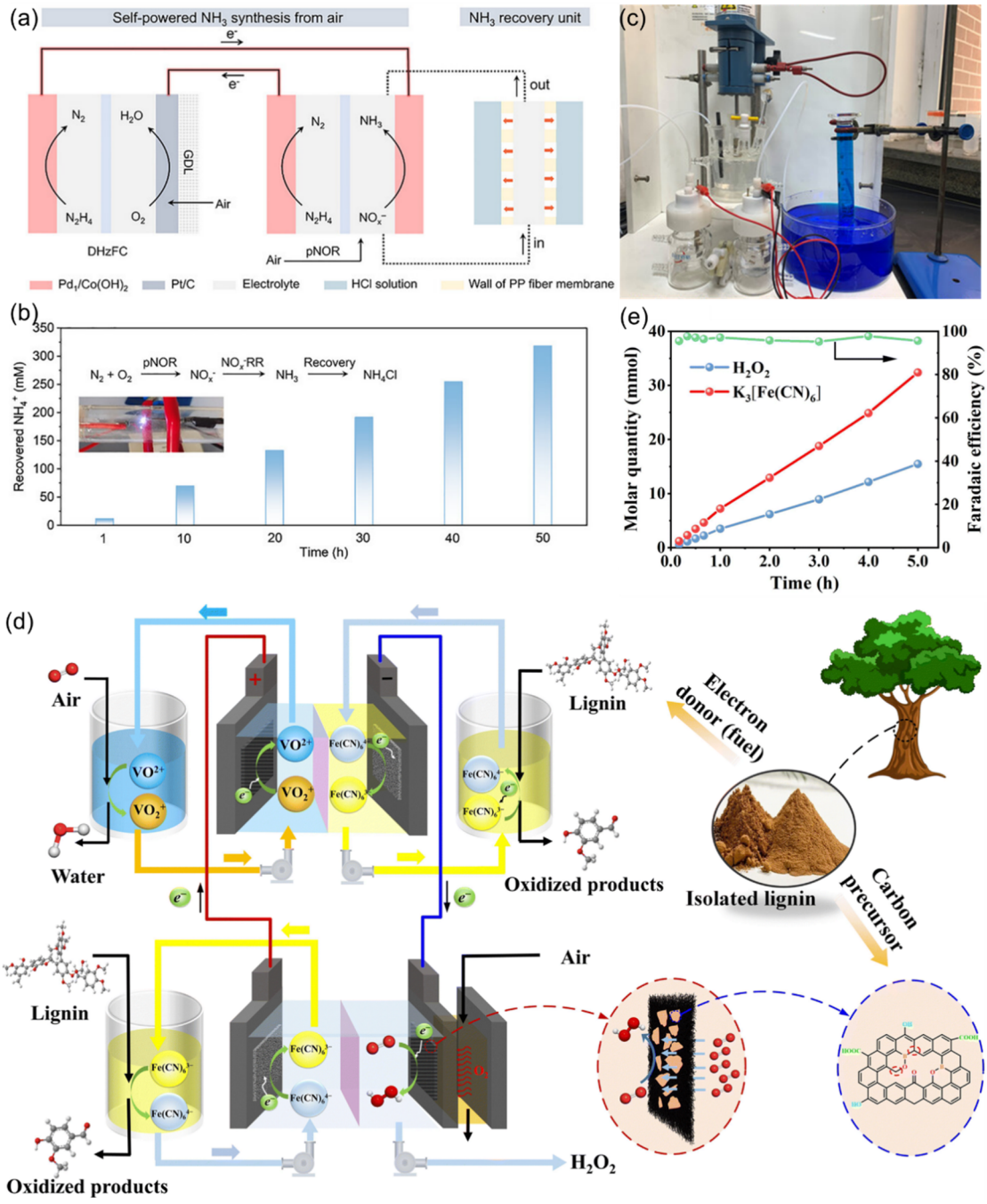

Figure 7. (**a**) Schematic of the pNOR-NO_x^-RR system and a NH_3 production system created by integrating a homemade DHzFC with a NNB unit. (**b**) The accumulated amount of NH_4^+ recovered by the flow-through coupled device during the stability test. Reproduced with permission. [194] Copyright 2025, John Wiley and Sons. (**c**) ZAB drive NO_3^-RR electrolytic system. Reproduced with permission. [197] Copyright 2025, John Wiley and Sons. (**d**) The coupled system developed in this work for electrochemical production of H_2O_2 with air as the oxygen source and lignin as a sustainable carbon precursor and electron donor. (**e**) The molar quantity of $[Fe(CN)_6]^{3-}$ in the anolyte of DLFC and H_2O_2 in the catholyte of the electrolytic cell during 5 h electrolysis. Reproduced with permission. [202] Copyright 2025, The Royal Society of Chemistry.

5. Conclusions, Challenges, and Perspectives

This Review has summarized recent advances in integrated aqueous electrochemical energy devices (IAEEDs), a dual-circuit driver–driven platform that couples internally powered energy-generating modules with electrocatalytic upgrading units for sustainable fuel and chemical production. Unlike conventional externally powered electrolysis, IAEEDs convert stored chemical energy directly into targeted products through modular aqueous electrochemical integration, offering potential advantages for decentralized, off-grid, and low-carbon chemical manufacturing. Nevertheless, the field is still dominated by proof-of-concept demonstrations. The key challenge is no longer simply whether a battery or fuel cell can power an electrosynthetic reaction, but whether the coupled system can maintain stable voltage/current matching, product selectivity, energy efficiency, and durability under realistic operating conditions. Future progress therefore requires a transition from catalyst-centered demonstrations to system-level engineering, with particular emphasis on source–load matching, interfacial mass transport, electrolyte/membrane compatibility, coupled degradation, stack design, product separation, and standardized full-device evaluation (Figure 8).

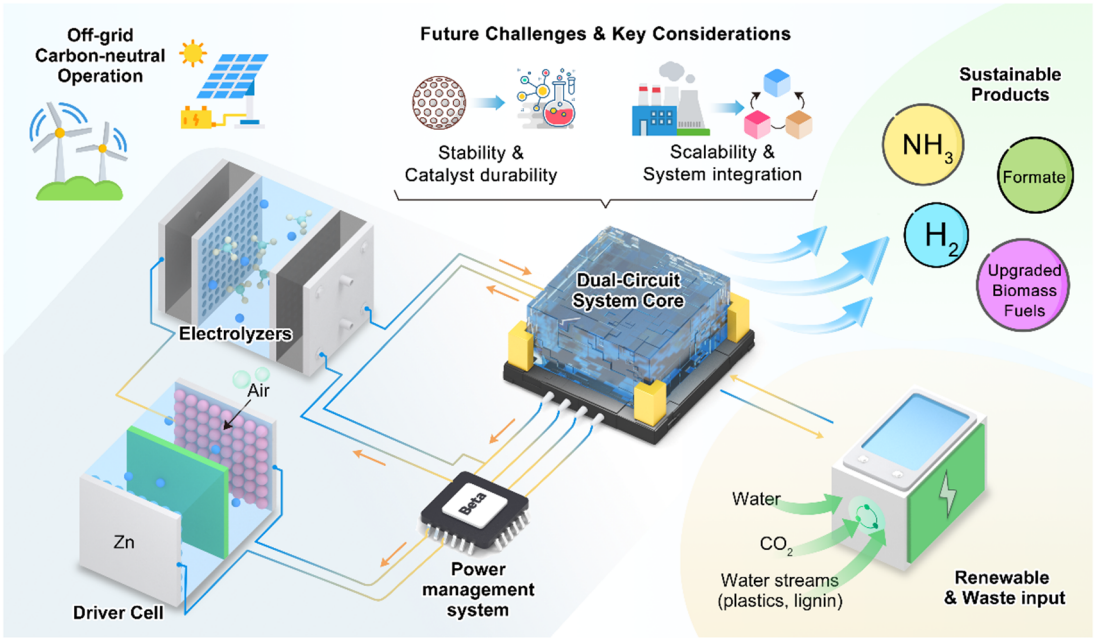

Figure 8. Illustration of challenges and perspectives for IAEEDs.

5.1. Scalability and Engineering Challenges

A major barrier to practical IAEEDs is that scale-up cannot be achieved by simply enlarging electrode area or connecting more battery/fuel-cell units to an electrolyzer. Instead, scalability requires coordinated engineering of the driver module, driven reactor, electrolyte/membrane environment, flow architecture, electrical connection, and downstream product-handling process.

First, stable source–load matching must be maintained during long-term operation. In IAEEDs, the operating current is determined by the dynamic intersection between the discharge curve of the driver module and the polarization curve of the driven module. Voltage decay in the driver cell, catalyst deactivation, membrane resistance growth, electrolyte depletion, gas-bubble accumulation, or product crossover can shift this operating point, leading to current decay, selectivity drift, and efficiency loss. Therefore, scalable IAEEDs should be designed through full-device polarization matching rather than by independently optimizing isolated half-cell catalysts.

Second, stack-level power distribution remains a critical engineering challenge. Series-connected driver modules can increase voltage for demanding reactions such as overall water splitting or multi-electron CO_2 reduction, whereas parallel-connected modules can increase current output and production rate. However, both strategies introduce risks of cell imbalance, uneven discharge, localized heating, increased contact resistance, and failure propagation. Future stack architectures should therefore integrate electrical balancing, current collectors, thermal management, sealing, pressure control, and diagnostic monitoring from the beginning.

Third, mass transport and gas/liquid management become increasingly difficult at larger scale. Enlarged electrodes and high current densities intensify concentration gradients, gas flooding, bubble blockage, electrolyte evaporation, pressure drop, and nonuniform reactant distribution. For gas-involving reactions, including ORR,

HER, CO_2RR, and fuel-cell reactions, the gas–liquid–solid interface must simultaneously enable efficient gas supply, ion transport, electron conduction, and product removal. Gas-diffusion electrodes, zero-gap reactors, membrane–electrode assemblies, and flow-cell architectures are promising for scale-up, but their long-term operation must address flooding, drying, carbonate precipitation, pressure imbalance, and local mass-transport failure.

Fourth, membrane, separator, and electrolyte compatibility must be solved at the system level. Membranes and separators are essential for ion transport, crossover suppression, and product purity, but they also introduce ohmic resistance and may suffer from swelling, dehydration, carbonate formation, fouling, or chemical degradation. Electrolyte selection is equally challenging because the optimal electrolyte for the driver circuit may not be compatible with the driven reaction. For example, alkaline media favor Zn–air batteries and many oxidation reactions, but carbonate formation can severely affect CO_2-related systems. Neutral or buffered electrolytes may improve CO_2RR selectivity but often suffer from lower conductivity and limited buffering capacity at high current density. Thus, scalable IAEEDs require electrolyte/membrane co-design rather than independent electrolyte selection for each half-reaction.

Fifth, product separation, electrolyte recycling, and safety management should be integrated into the device architecture. Products such as H_2, CO, formate, ammonia, hydrogen peroxide, and biomass-derived chemicals often require downstream separation, purification, or concentration, which can substantially change the real system efficiency and economic feasibility. In addition, Zn metal, hydrazine, ammonia, CO-containing gas streams, concentrated alkaline electrolytes, and pressurized gases introduce safety and handling concerns. Therefore, practical IAEEDs should be evaluated as process-integrated systems rather than isolated electrochemical cells.

5.2. Actionable Research Priorities and Emerging Opportunities

To move IAEEDs from laboratory demonstrations toward practical technologies, future studies should focus on several specific and actionable research priorities.

First, standardized full-device benchmarking should be established. Future reports should include driver discharge curves, driven-cell polarization curves, matched operating voltage and current, power output, product formation rate, Faradaic efficiency, energy efficiency, product selectivity retention, and long-term stability under continuous coupled operation. A current-matching coefficient or source–load matching descriptor could be introduced to quantify how effectively the driver output is utilized by the driven reaction. Such metrics would enable meaningful comparison among different IAEED configurations and avoid overestimating performance based only on isolated half-cell data.

Second, dynamic source–load matching should become a core design principle. Instead of simply connecting a battery or fuel cell to an electrolyzer, future systems should be designed through polarization matching maps under different electrolyte concentrations, flow rates, electrode areas, temperatures, and reactant feeds. For high-voltage reactions, such as water splitting and multi-electron CO_2 reduction, series-connected driver modules may be required; for high-rate production, parallel or hybrid series–parallel architectures should be optimized. This strategy would transform empirical device assembly into rational electrochemical system design.

Third, operando diagnostics under real coupled operation should become routine. Most mechanistic studies are still performed in isolated three-electrode configurations, which cannot fully capture voltage fluctuation, current drift, local pH variation, crossover, or coupled degradation in IAEEDs. Operando X-ray absorption spectroscopy, Raman spectroscopy, infrared spectroscopy, electrochemical impedance spectroscopy, pH mapping, gas analysis, and electrolyte composition tracking should be applied during actual driver–driven operation. These tools can reveal catalyst reconstruction, membrane degradation, charge-transfer resistance growth, carbonate formation, gas blockage, and product crossover.

Fourth, electrolyte, membrane, and interface co-design should be prioritized. Electrolytes in IAEEDs are not passive ion conductors; they regulate local pH, ionic conductivity, interfacial electric fields, catalyst reconstruction, product crossover, and membrane stability. Emerging opportunities include asymmetric electrolytes, bipolar membranes, ion-selective separators, localized electrolyte engineering, and controlled flow-electrolyte systems. These strategies should be developed to balance conductivity, selectivity, stability, and product separation in specific driver–driven pairs.

Fifth, modular and stackable reactor architectures should be developed for practical current and production rates. Promising configurations include zero-gap reactors, membrane–electrode assemblies, gas-diffusion electrodes, modular flow cells, and integrated driver–driven stacks. These systems should be tested under enlarged electrode areas, continuous electrolyte circulation, realistic reactant feeds, and extended operation. The evaluation target should shift from short-term high activity to stable production rate, high energy efficiency, reproducible module-to-module performance, and long-term durability.

Sixth, reaction-pairing strategies should be expanded toward high-value and waste-derived feedstocks. Beyond water splitting and CO_2 reduction, emerging opportunities include coupling hydrogen production or CO_2 conversion with biomass-derived alcohol oxidation, plastic-derived intermediates, sulfide-containing wastewater, nitrate/nitrite streams, urea-rich wastewater, and other industrial effluents. These pairings can reduce thermodynamic energy demand while producing valuable chemicals or enabling waste remediation. However, future studies should carefully evaluate feedstock availability, catalyst poisoning, electrolyte contamination, product separation, and economic value, rather than selecting alternative reactions only because they have lower thermodynamic potentials.

Seventh, autonomous control and digital optimization should be introduced into IAEED development. Because driver output and driven reaction demand evolve continuously during operation, static device design may not maintain optimal performance over long time scales. Voltage/current sensors, impedance monitoring, flow-rate control, and feedback algorithms could be integrated to regulate reactant supply, electrolyte circulation, module connection, and product removal. Digital twins and machine-learning-assisted optimization may help predict operating-point drift, identify early-stage failure, and optimize source–load matching in modular IAEED stacks.

Finally, techno-economic analysis and life-cycle assessment should be incorporated at the early design stage. High Faradaic efficiency or low operating voltage does not necessarily guarantee practical value if the system requires expensive membranes, hazardous fuels, complex separation, or short component lifetime. Future studies should quantify capital cost, material utilization, product separation energy, carbon footprint, safety requirements, and device lifetime. At present, low-voltage hydrogen production coupled with waste or biomass oxidation and fuel-cell-driven selective organic upgrading appear relatively closer to practical translation, whereas self-driven CO_2-to-multicarbon production and ammonia synthesis remain less mature because of their stringent voltage, selectivity, mass-transport, and separation requirements.

In summary, IAEEDs represent an emerging platform at the interface of electrochemical energy conversion, catalysis, device engineering, and sustainable chemical manufacturing. Their future development should move beyond isolated catalyst optimization toward integrated system design, where electrode materials, electrolytes, membranes, interfaces, source–load matching, stack architecture, diagnostics, and process engineering are optimized together. With standardized benchmarking, durable coupled systems, scalable device architectures, and economically meaningful reaction pairings, dual-circuit aqueous electrochemical devices may evolve from laboratory demonstrations into practical platforms for decentralized, low-carbon, and value-added production of fuels and chemicals.

Funding

The authors gratefully acknowledge valuable discussions from colleagues in the field. This work was financially supported by the National Key Research & Development Program of China (2022YFE0115900, 2023YFA1507101, 2021YFA1501500), the National Natural Science Foundation of China (No. 22225902, U22A20436, No. 22409171), the Self-deployment Project Research Program of Haixi Institutes, Chinese Academy of Sciences (No. CXZX-2022-GH04, CXZX-2023-JQ08), and the Postdoctoral Fellowship Program of CPSF (No. GZC20241720). Science and Technology Program of Fuzhou (2023-P-009).

Conflicts of Interest

The authors declare no conflict of interest. Given the role as Editorial Board Member, Zhenhai Wen had no involvement in the peer review of this paper and had no access to information regarding its peer-review process. Full responsibility for the editorial process of this paper was delegated to another editor of the journal.

Use of AI and AI-Assisted Technologies

During the preparation of this work, the authors used Chatgpt to revise the grammars. After using this tool/service, the authors reviewed and edited the content as needed and takes full responsibility for the content of the published article.

References

1. Belaïd, F.; Al-Sarihi, A.; Al-Mestneer, R. Balancing climate mitigation and energy security goals amid converging global energy crises: The role of green investments. *Renew. Energy* **2023**, *205*, 534–542. https://doi.org/10.1016/j.renene.2023.01.083.
2. Li, W.; Liu, J.; Zhao, D. Mesoporous materials for energy conversion and storage devices. *Nat. Rev. Mater.* **2016**, *1*, 16023. https://doi.org/10.1038/natrevmats.2016.23.

3. Slameršak, A.; Kallis, G.; O'Neill, D.W. Energy requirements and carbon emissions for a low-carbon energy transition. *Nat. Commun.* **2022**, *13*, 6932. https://doi.org/10.1038/s41467-022-33976-5.
4. Montoya, J.H.; Seitz, L.C.; Chakthranont, P.; et al. Materials for solar fuels and chemicals. *Nat. Mater.* **2017**, *16*, 70–81. https://doi.org/10.1038/nmat4778.
5. Chen, S.; Xiao, X.; Li, Z.; et al. The perspective of offshore wind power: based hydrogen production, hydrogen storage, and hydrogen transportation. *Mater. Today* **2025**, *90*, 800–814. https://doi.org/10.1016/j.mattod.2025.09.016.
6. Tang, C.; Zheng, Y.; Jaroniec, M.; et al. Electrocatalytic refinery for sustainable production of fuels and chemicals. *Angew. Chem. Int. Ed.* **2021**, *60*, 19572–19590.
7. Tu, Q.; Parvatker, A.; Garedew, M.; et al. Electrocatalysis for chemical and fuel production, investigating climate change mitigation potential and economic feasibility. *Environ. Sci. Technol.* **2021**, *55*, 3240–3249. https://doi.org/10.1021/acs.est.0c07309.
8. Xia, Y.; Zhang, L.; Hu, B.; et al. Design of highly-active photocatalytic materials for solar fuel production. *Chem. Eng. J.* **2021**, *421*, 127732.
9. Hu, F.; Chen, K.; Lu, Z.; et al. Self-powered electrocatalytic aldehyde reforming fuel cell for sustainable H_2 Generation with ∼200% Faradaic efficiency. *Angew. Chem. Int. Ed.* **2025**, *64*, e202504894.
10. Cao, X.; Jie, Y.; Wang, N.; et al. Triboelectric nanogenerators driven self-powered electrochemical processes for energy and environmental science. *Adv. Energy Mater.* **2016**, *6*, 1600665. https://doi.org/10.1002/aenm.201600665.
11. Yang, R.; Zheng, X.; Qin, M.; et al. A Trifunctional Ni–P/Fe–P collaborated electrocatalyst enables self-powered energy systems. *Adv. Sci.* **2022**, *9*, 2201594.
12. Ren, J.T.; Chen, L.; Wang, H.Y.; et al. Water electrolysis for hydrogen production, from hybrid systems to self-powered/catalyzed devices. *Energy Environ. Sci.* **2024**, *17*, 49–113. https://doi.org/10.1039/d3ee02467a.
13. Khan, M.A.; Al-Shankiti, I.; Ziani, A.; et al. A stable integrated photoelectrochemical reactor for H_2 production from water attains a solar-to-hydrogen efficiency of 18% at 15 suns and 13% at 207 suns. *Angew. Chem. Int. Ed.* **2020**, *59*, 14802–14808.
14. Hao, X.; Yang, Q.; Zhuo, X.; et al. Trifunctional phosphorus-doped cobalt molybdate catalyst in self-driven coupling systems for synchronized sulfur recovery and hydrogen evolution. *J. Colloid. Interface Sci.* **2024**, *674*, 145–157. https://doi.org/10.1016/j.jcis.2024.06.051.
15. Amstutz, V.; Toghill, K.E.; Powlesland, F.; et al. Renewable hydrogen generation from a dual-circuit redox flow battery. *Energy Environ. Sci.* **2014**, *7*, 2350–2358. https://doi.org/10.1039/c4ee00098f.
16. Kin, L.C.; Astakhov, O.; Lee, M.; et al. Batteries to keep solar-driven water splitting running at night, performance of a directly coupled system. *Sol. RRL* **2022**, *6*, 2100916. https://doi.org/10.1002/solr.202100916.
17. Zhang, P.; Wei, M.; Wang, K.; et al. Performance optimization of zinc-air batteries via nanomaterials. *Energy Storage Mater.* **2025**, *75*, 104109. https://doi.org/10.1016/j.ensm.2025.104109.
18. Gupta, D.; Mao, J.; Guo, Z. Bifunctional catalysts for CO_2 reduction and O_2 evolution, a pivotal for aqueous rechargeable Zn-CO2 batteries. *Adv. Mater.* **2024**, *36*, 2407099. https://doi.org/10.1002/adma.202407099.
19. Huang, R.B.; Wang, M.Y.; Xiong, J.F.; et al. Anode optimization strategies for zinc-air batteries. *eScience* **2025**, *5*, 100309. https://doi.org/10.1016/j.esci.2024.100309.
20. Li, Y.; Xu, J.; Lan, F.; et al. Atomic-level tin regulation for high-performance Zinc–air batteries. *J. Am. Chem. Soc.* **2025**, *147*, 4833–4843.
21. Yang, Y.; Liu, J.; Ahmad, M. Dual Hydrogen-producing formaldehyde-water fuel cell for pollutant treatment and valuable chemical Co-generation.; et al. *Chem. Eng. J.* **2025**, *505*, 159653.
22. Chen, L.; Yu, C.; Dong, J.; et al. Seawater electrolysis for fuels and chemicals production, fundamentals, achievements, and perspectives. *Chem. Soc. Rev.* **2024**, *53*, 7455–7488. https://doi.org/10.1039/d3cs00822c.
23. Zhao, H.; Yuan, Z.Y. Self-powered electrochemical energy systems to produce fuels. *Mater. Horiz.* **2025**, *12*, 4027–4041. https://doi.org/10.1039/d5mh00285k.
24. Jia, P.; Yu, Y.; Chen, T.; et al. "Electricity"-assisted catalytic solar-to-fuel processes. *Angew. Chem. Int. Ed.* **2025**, *64*, e202508809.
25. Song, C.; Xuan, N.; Du, X.; et al. Self-powered electrocatalytic integrated system based on TENG for high-yield bipolar hydrogen production. *Nano Energy* **2025**, *136*, 110707. https://doi.org/10.1016/j.nanoen.2025.110707.
26. Domenici, S.; Speranza, R.; Bella, F.; et al. A sustainable hydrogel-based dye-sensitized solar cell coupled to an integrated supercapacitor for direct indoor light-energy storage. *Sol. RRL* **2025**, *9*, 2400838. https://doi.org/10.1002/solr.202400838.
27. Feng, Y.; Zhang, Z.; Gao, Z.; et al. Tailoring lewis acidity of nanoporous V-doped Co_2P for self-powered hydrazine-water splitting. *Adv. Energy. Mater.* **2026**, e71101. https://doi.org/10.1002/aenm.71101.
28. Liu, X.; Yuan, Y.; Liu, J.; et al. Utilizing solar energy to improve the oxygen evolution reaction kinetics in zinc-air battery. *Nat. Commun.* **2019**, *10*, 4767. https://doi.org/10.1038/s41467-019-12627-2.
29. Huang, Y.; Zhang, X.; Li, L.; et al. Mott-Schottky barrier enabling high-performance hydrazine-assisted hydrogen generation at ampere-level current densities. *Adv. Funct. Mater.* **2025**, *35*, 2401011. https://doi.org/10.1002/adfm.202401011.

30. Tang, L.; Peng, H.; Kang, J.; et al. Zn-based batteries for sustainable energy storage, strategies and mechanisms. *Chem. Soc. Rev.* **2024**, *53*, 4877–4925. https://doi.org/10.1039/d3cs00295k.
31. Zou, X.; Tang, M.; Lu, Q.; et al. Carbon-based electrocatalysts for rechargeable Zn-air batteries, design concepts, recent progress and future perspectives. *Energy Environ. Sci.* **2024**, *17*, 386–424. https://doi.org/10.1039/d3ee03059h.
32. Zhou, T.; Zhang, N.; Wu, C.; et al. Surface/interface nanoengineering for rechargeable Zn-air batteries. *Energy Environ. Sci.* **2020**, *13*, 1132–1153. https://doi.org/10.1039/c9ee03634b.
33. Wang, L.; Huang, W.; Guo, W.; et al. Sn alloying to inhibit hydrogen evolution of Zn metal anode in rechargeable aqueous batteries. *Adv. Funct. Mater.* **2022**, *32*, 2108533. https://doi.org/10.1002/adfm.202108533.
34. Su, K.; Zhang, X.; Zhang, X.; et al. Polar small molecular electrolyte additive for stabilizing Zn anode. *Chem. Eng. J.* **2023**, *474*, 145730.
35. Wang, S.; Zhang, M.; Mu, X.; et al. Atomically dispersed multi-site catalysts, bifunctional oxygen electrocatalysts boost flexible zinc-air battery performance. *Energy Environ. Sci.* **2024**, *17*, 4847–4870. https://doi.org/10.1039/d4ee01656d.
36. Zeng, K.; Zheng, X.; Li, C.; et al. Recent advances in non-noble bifunctional oxygen electrocatalysts toward large-scale production. *Adv. Funct. Mater.* **2020**, *30*, 2000503. https://doi.org/10.1002/adfm.202000503.
37. Zhou, G.; Liu, G.; Liu, X.; et al. 1D/3D heterogeneous assembling body as trifunctional electrocatalysts enabling zinc-air battery and self-powered overall water splitting. *Adv. Funct. Mater.* **2022**, *32*, 2107608. https://doi.org/10.1002/adfm.202107608.
38. Zhang, Z.; Zhao, X.; Xi, S.; et al. Atomically dispersed cobalt trifunctional electrocatalysts with tailored coordination environment for flexible rechargeable Zn-air battery and self-driven water splitting. *Adv. Energy Mater.* **2020**, *10*, 2002896. https://doi.org/10.1002/aenm.202002896.
39. Huang, L.; Zaman, S.; Tian, X.; et al. Advanced platinum-based oxygen reduction electrocatalysts for fuel cells. *Acc. Chem. Res.* **2021**, *54*, 311–322.
40. Wang, X.X.; Swihart, M.T.; Wu, G. Achievements, challenges and perspectives on cathode catalysts in proton exchange membrane fuel cells for transportation. *Nat. Catal.* **2019**, *2*, 578–589. https://doi.org/10.1038/s41929-019-0304-9.
41. Xiao, F.; Wang, Y.C.; Wu, Z.P.; et al. Recent advances in electrocatalysts for proton exchange membrane fuel cells and alkaline membrane fuel cells. *Adv. Mater.* **2021**, *33*, 2006292. https://doi.org/10.1002/adma.202006292.
42. Ren, J.T.; Chen, L.; Wang, H.Y.; et al. Hydrogen oxidation electrocatalysts for anion-exchange membrane fuel cells, activity descriptors, stability regulation, and perspectives. *Energy Environ. Sci.* **2024**, *17*, 3960–4009. https://doi.org/10.1039/d3ee04251k.
43. Alfaifi, S.M.; Balu, R.; Chiang, K.; et al. Electrocatalysts for the oxygen reduction reaction in proton exchange membrane fuel cells, significant advances, major challenges, and future directions. *ACS Catal.* **2025**, *15*, 9301–9345. https://doi.org/10.1021/acscatal.5c00903.
44. Burshtein, T.Y.; Yasman, Y.; Muñoz-Moene, L.; et al. Hydrazine oxidation electrocatalysis. *ACS Catal.* **2024**, *14*, 2264–2283. https://doi.org/10.1021/acscatal.3c05657.
45. Gao, L.; Sun, H.; Sun, H.; et al. Embedding Ru single atom catalysts on Co_3O_4 for efficient hydrazine oxidation and direct hydrazine fuel cells. *Appl. Catal. B Environ. Energy* **2024**, *358*, 124287. https://doi.org/10.1016/j.apcatb.2024.124287.
46. Yu, Y.; Lee, S.J.; Theerthagiri, J.; et al. Architecting the AuPt alloys for hydrazine oxidation as an anolyte in fuel cell, comparative analysis of hydrazine splitting and water splitting for energy-saving H2 generation. *Appl. Catal. B Environ.* **2022**, *316*, 121603. https://doi.org/10.1016/j.apcatb.2022.121603.
47. Sun, H.; Gao, L.; Kumar, A.; et al. Superaerophobic CoP nanowire arrays as a highly effective anode electrocatalyst for direct hydrazine fuel cells. *ACS Appl. Energy Mater.* **2022**, *5*, 9455–9462. https://doi.org/10.1021/acsaem.2c01005.
48. Chatenet, M.; Pollet, B.G.; Dekel, D.R.; et al. Water electrolysis, from textbook knowledge to the latest scientific strategies and industrial developments. *Chem. Soc. Rev.* **2022**, *51*, 4583–4762. https://doi.org/10.1039/d0cs01079k.
49. Liu, D.; Xu, G.; Yang, H.; et al. Rational design of transition metal phosphide-based electrocatalysts for hydrogen evolution. *Adv. Funct. Mater.* **2023**, *33*, 2208358. https://doi.org/10.1002/adfm.202208358.
50. Wang, M.; Zhang, L.; He, Y.; et al. Recent advances in transition-metal-sulfide- based bifunctional electrocatalysts for overall water splitting. *J. Mater. Chem. A* **2021**, *9*, 5320–5363.
51. Jin, H.; Wang, X.; Tang, C.; et al. Stable and highly efficient hydrogen evolution from seawater enabled by an unsaturated nickel surface nitride. *Adv. Mater.* **2021**, *33*, 2007508. https://doi.org/10.1002/adma.202007508.
52. Yang, C.; Shen, K.; Zhao, R.; et al. Balance effect, a universal strategy for transition metal carbides to enhance hydrogen evolution. *Adv. Funct. Mater.* **2022**, *32*, 2108167. https://doi.org/10.1002/adfm.202108167.
53. Wang, Y.; Zhang, M.; Liu, Y.; et al. Recent advances on transition-metal-based layered double hydroxides nanosheets for electrocatalytic energy conversion. *Adv. Sci.* **2023**, *10*, 2207519.
54. Li, M.; Li, H.; Fan, H.; et al. Engineering interfacial sulfur migration in transition-metal sulfide enables low overpotential for durable hydrogen evolution in seawater. *Nat. commun* **2024**, *15*, 6154. https://doi.org/10.1038/s41467-024-50535-2.

55. Zhang, H.; Wu, Y.; Wang, X.; et al. The construction of defect-rich CoP@ CoP@(Co/Ni)$_2$P triple-shell hollow nanospheres with boosted electrocatalytic hydrogen evolution performances over a wide pH range. *Chem. Eng. J.* **2023**, *463*, 142448.
56. Fu, Q.; Wong, L.W.; Zheng, F.; et al. Unraveling and leveraging in situ surface amorphization for enhanced hydrogen evolution reaction in alkaline media. *Nat. Commun.* **2023**, *14*, 6462. https://doi.org/10.1038/s41467-023-42221-6.
57. Ning, M.; Wang, Y.; Wu, L.; et al. Hierarchical interconnected NiMoN with large specific surface area and high mechanical strength for efficient and stable alkaline water/seawater hydrogen evolution. *Nano-Micro Lett.* **2023**, *15*, 157. https://doi.org/10.1007/s40820-023-01129-y.
58. Monteiro, M.C.; Philips, M.F.; Schouten, K.J.P.; et al. Efficiency and selectivity of CO_2 reduction to CO on gold gas diffusion electrodes in acidic media. *Nat. Commun.* **2021**, *12*, 4943. https://doi.org/10.1038/s41467-021-24936-6.
59. Zhang, Z.; Yang, Z.; Liu, L.; et al. Catalytic CO_2 conversion to C1 chemicals over single-atom catalysts. *Adv. Energy Mater.* **2023**, *13*, 2301852. https://doi.org/10.1002/aenm.202301852.
60. Peramaiah, K.; Yi, M.; Dutta, I.; et al. Catalyst design and engineering for CO_2-to-formic acid electrosynthesis for a low-carbon economy. *Adv. Mater.* **2024**, *36*, 2404980. https://doi.org/10.1002/adma.202404980.
61. Cai, J.; Zhao, Q.; Hsu, W.Y. Highly selective electrochemical reduction of CO_2 into methane on nanotwinned Cu. *J. Am. Chem. Soc.* **2023**, *145*, 9136–9143.
62. Zheng, M.; Zhang, J.; Wang, P.; et al. Recent advances in electrocatalytic hydrogenation reactions on copper-based catalysts. *Adv. Mater.* **2024**, *36*, 2307913. https://doi.org/10.1002/adma.202307913.
63. Yao, K.; Li, J.; Ozden, A.; et al. In situ copper faceting enables efficient CO_2/CO electrolysis. *Nat. Commun.* **2024**, *15*, 1749. https://doi.org/10.1038/s41467-024-45538-y.
64. Li, H.; Liu, T.; Wei, P.; et al. High-rate CO_2 electroreduction to C_{2+} products over a copper-copper iodide catalyst. *Angew. Chem. Int. Ed.* **2021**, *133*, 14450–14454.
65. Zheng, M.; Wang, P.; Zhi, X.; et al. Electrocatalytic CO_2-to-C_{2+} with ampere-level current on heteroatom-engineered copper via tuning *CO intermediate coverage. *J. Am. Chem. Soc.* **2022**, *144*, 14936–14944.
66. Wang, F.; Lu, Z.; Guo, H.; et al. Copper-based catalysts for CO_2 electroreduction to C_2/$_{2+}$ products, Advance and perspective. *Coord. Chem. Rev.* **2024**, *515*, 215962. https://doi.org/10.1016/j.ccr.2024.215962.
67. Luo, H.; Barrio, J.; Sunny, N.; et al. Progress and perspectives in photo- and electrochemical-oxidation of biomass for sustainable chemicals and hydrogen production. *Adv. Energy Mater.* **2021**, *11*, 2101180. https://doi.org/10.1002/aenm.202101180.
68. Zheng, M.; Wang, P.; Gao, Y.; et al. Tuning interfacial *H coverage and aldehyde adsorption configuration for selective electrocatalytic hydrogenation of furfural. *J. Mater. Chem. A* **2025**, *13*, 9135–9143.
69. Xu, C.; Paone, E.; Rodríguez-Padrón, D.; et al. Recent catalytic routes for the preparation and the upgrading of biomass derived furfural and 5-hydroxymethylfurfural. *Coord. Chem. Rev.* **2020**, *49*, 4273–4306.
70. Yoo, M.; Choi, D.; Shin, M.; et al. Selective electrocatalytic oxidation of glycerol to high-value C_1–C_3 products, From chemistry to scalability. *Chem. Eng. J.* **2025**, *518*, 164743.
71. Fan, L.; Ji, Y.; Wang, G.; et al. High entropy alloy electrocatalytic electrode toward alkaline glycerol valorization coupling with acidic hydrogen production. *J. Am. Chem. Soc.* **2022**, *144*, 7224–7235.
72. Gao, Y.; Ge, L.; Xu, H.; et al. Electrocatalytic refinery of biomass-based 5-hydroxymethylfurfural to fine chemicals. *ACS Catal.* **2023**, *13*, 11204–11231. https://doi.org/10.1021/acscatal.3c02272.
73. Peng, Q.; Fang, W.; Li, D.; et al. Materials designs for selective electrocatalytic HMF reduction to BHMF and perspectives. *Chem. Commun.* **2026**, *62*, 2492–2510. https://doi.org/10.1039/d5cc06202k.
74. Zhu, P.; Shi, M.; Shen, Z.; et al. Electrocatalytic conversion of biomass-derived furan compounds, mechanisms, catalysts and perspectives. *Chem. Sci.* **2024**, *15*, 4723–4756. https://doi.org/10.1039/d4sc00546e.
75. Tan, M.; Hua, Q.; Zhang, C.; et al. Creating abundant gas-solid-liquid triple-phase interfaces in hierarchical porous structure for efficient electrochemical CO_2 reduction. *Adv. Funct. Mater.* **2025**, *35*, 2510570. https://doi.org/10.1002/adfm.202510570.
76. Abbasi, A.; Xu, Y.; Khezri, R.; et al. Advances in characteristics improvement of polymeric membranes/separators for zinc-air batteries. *Mater. Today Sustain.* **2022**, *18*, 100126. https://doi.org/10.1016/j.mtsust.2022.100126.
77. Song, W.; Sun, Z.; Guo, M.; et al. Novel high-safety composite separator, achieving efficient alkaline water electrolysis by compositing microporous polysulfone membrane on one side of complete structure polyphenylene sulfide fabric. *Chem. Eng. J.* **2025**, *503*, 158688.
78. Qu, J.; Wang, Z.; Gan, W.; et al. Efficient hydrogen evolution on antiperovskite $CuNCo_3$ nanowires by Mo incorporation and its trifunctionality for Zn air batteries and overall water splitting. *Small* **2024**, *20*, 2304541. https://doi.org/10.1002/smll.202304541.
79. Xu, H.; Chen, L.; Shi, J. Advanced electrocatalytic systems for enhanced atom/electron utilization. *Energy Environ. Sci.* **2023**, *16*, 1334–1363. https://doi.org/10.1039/d2ee03323b.

80. Kim, D.W.; Kim, J.; Choi, J.H.; et al. Trifunctional graphene-sandwiched heterojunction-embedded layered lattice electrocatalyst for high performance in Zn-air battery-driven water splitting. *Adv. Sci.* **2024**, *11*, 2408869.
81. Surendran, S.; Lim, Y.; Lee, S.; et al. Understanding the engineering tactics to achieve the stabilized anode in next-generation Zn-air batteries. *Exploration* **2025**, *5*, 20240054. https://doi.org/10.1002/exp.20240054.
82. Wei, J.; Lou, J.; Hu, W.; et al. Superstructured carbon with enhanced kinetics for Zinc-air battery and self-powered overall water splitting. *Small* **2024**, *20*, 2308956.
83. Zhang, M.; Li, H.; Chen, J.; et al. A low-cost, durable bifunctional electrocatalyst containing atomic Co and Pt species for flow alkali-Al/acid hybrid fuel cell and Zn-air battery. *Adv. Funct. Mater.* **2023**, *33*, 2303189. https://doi.org/10.1002/adfm.202303189.
84. Wang, X.; Zhou, X.; Li, C.; et al. Asymmetric Co-N_3P_1 trifunctional catalyst with tailored electronic structures enabling boosted activities and corrosion resistance in an uninterrupted seawater splitting system. *Adv. Mater.* **2022**, *34*, 2204021. https://doi.org/10.1002/adma.202204021.
85. Zhang, J.; Dai, L. Nitrogen, phosphorus, and fluorine tri-doped graphene as a multifunctional catalyst for self-powered electrochemical water splitting. *Angew. Chem. Int. Ed.* **2016**, *128*, 13490–13494.
86. Muthurasu, A.; Pathak, I.; Acharya, D.; et al. Cutting-edge nitrogen, boron, and fluorine triply doped chain-like porous carbon nanofibers, a versatile solution for high-performance zinc-air batteries and self-powered water splitting. *J. Mater. Chem. A* **2024**, *12*, 1826–1839.
87. Liu, W.; Bao, J.; Xu, L.; et al. Chromium-modulated multifunctional electrocatalytic activities of spinel oxide for Zn-air batteries and overall water splitting. *J. Power Sources* **2020**, *479*, 229099. https://doi.org/10.1016/j.jpowsour.2020.229099.
88. Zheng, X.; Wang, Z.; Zeng, D.; et al. $NiFe_2O_4$ nanoflowers with Mo doping for self-powered hydrogen production at large current density. *J. Mater. Chem. C* **2025**, *13*, 9099–9105.
89. Jian, J.; Nie, P.; Wang, Z.; et al. V^{5+}-doped potassium ferrite as an efficient trifunctional catalyst for large-current-density water splitting and long-life rechargeable Zn-air battery. *ACS Appl. Mater. Interfaces* **2022**, *14*, 36721–36730. https://doi.org/10.1021/acsami.2c09725.
90. Wang, M.; Su, K.; Zhang, M.; et al. Advanced trifunctional electrocatalysis with Cu-, N-, S-doped defect-rich porous carbon for rechargeable Zn-air batteries and self-driven water splitting. *ACS Sustainable Chem. Eng.* **2021**, *9*, 13324–13336. https://doi.org/10.1021/acssuschemeng.1c04745.
91. Zheng, X.; Zuria, A.M.; Mohamedi, M.J.A.E. Tailored self-supported Co, Ni/MnO_2 nanorods@ hierarchical carbon spheres chains as advanced electrocatalysts for rechargeable Zn-air battery and self-driven water splitting. *ACS Electrochem.* **2024**, *1*, 216–229.
92. Ge, H.; Li, G.; Shen, J.; et al. Co_4N nanoparticles encapsulated in N-doped carbon box as tri-functional catalyst for Zn-air battery and overall water splitting. *Appl. Catal. B Environ.* **2020**, *275*, 119104. https://doi.org/10.1016/j.apcatb.2020.119104.
93. Jin, Q.; Ren, B.; Cui, H.; et al. Nitrogen and cobalt co-doped carbon nanotube films as binder-free trifunctional electrode for flexible zinc-air battery and self-powered overall water splitting. *Appl. Catal. B Environ.* **2021**, *283*, 119643. https://doi.org/10.1016/j.apcatb.2020.119643.
94. Sun, Y.; Huang, B.; Li, Y.; et al. Trifunctional fishbone-like PtCo/Ir enables high-performance zinc–air batteries to drive the water-splitting catalysis. *Chem. Mater.* **2019**, *31*, 8136–8144. https://doi.org/10.1021/acs.chemmater.9b02892.
95. Lai, C.; Fang, J.; Liu, X.; et al. In situ coupling of NiFe nanoparticles with N-doped carbon nanofibers for Zn-air batteries driven water splitting. *Appl. Catal. B Environ.* **2021**, *285*, 119856. https://doi.org/10.1016/j.apcatb.2020.119856.
96. Yang, M.; Liu, Y.; Sun, J.; et al. Integration of partially phosphatized bimetal centers into trifunctional catalyst for high-performance hydrogen production and flexible Zn-air battery. *Sci. China Mater.* **2022**, *65*, 1176–1186. https://doi.org/10.1007/s40843-021-1902-2.
97. Yang, X.; Mao, H.; Zhou, Z.; et al. Biphasic nanoalloys-based trifunctional monolith for high-performance flexible Zn-air batteries and self-driven water splitting. *Adv. Funct. Mater.* **2024**, *34*, 2402933.
98. Ramakrishnan, S.; Balamurugan, J.; Vinothkannan, M.; et al. Nitrogen-doped graphene encapsulated FeCoMoS nanoparticles as advanced trifunctional catalyst for water splitting devices and zinc–air batteries. *Appl. Catal. B Environ.* **2020**, *279*, 119381. https://doi.org/10.1016/j.apcatb.2020.119381.
99. Lu, Z.; Sun, W.; Cai, P.; et al. High-entropy alloy catalysts for advanced hydrogen-production zinc-based batteries. *Energy Environ. Sci.* **2025**, *18*, 2918–2930. https://doi.org/10.1039/d4ee05500d.
100. Mondal, P.; Baitalik, S. Synergistic influence of multivalent $Ru^{\delta+}$ on a CeO_x nanocatalyst for self-powered efficient electrochemical water splitting. *J. Mater. Chem. A* **2025**, *13*, 368–386.
101. Feng, W.; Feng, Y.; Chen, J.; et al. Interfacial electronic engineering of Ru/FeRu nanoparticles as efficient trifunctional electrocatalyst for overall water splitting and Zn-air battery. *Chem. Eng. J.* **2022**, *437*, 135456.
102. Yin, J.; Li, Y.; Lv, F.; et al. Oxygen vacancies dominated NiS_2/CoS_2 interface porous nanowires for portable Zn-air batteries driven water splitting devices. *Adv. Mater.* **2017**, *29*, 1704681. https://doi.org/10.1002/adma.201704681.

103. Shi, Q.; Liu, Q.; Ma, Y.; et al. High-performance trifunctional electrocatalysts based on FeCo/Co_2P hybrid nanoparticles for zinc-air battery and self-powered overall water splitting. *Adv. Energy Mater.* **2020**, *10*, 1903854. https://doi.org/10.1002/aenm.201903854.
104. Zhang, L.; Zhu, Y.; Nie, Z.; et al. Co/MoC nanoparticles embedded in carbon nanoboxes as robust trifunctional electrocatalysts for a Zn-air battery and water electrocatalysis. *ACS Nano* **2021**, *15*, 13399–13414. https://doi.org/10.1021/acsnano.1c03766.
105. Hu, X.; Yang, T.; Yang, Z.; et al. Engineering of Co_3O_4@Ni_2P heterostructure as trifunctional electrocatalysts for rechargeable zinc-air battery and self-powered overall water splitting. *J. Mater. Sci. Technol.* **2022**, *115*, 19–28.
106. Kumar, M.; Nagaiah, T.C. A NiCu-MoS_2 electrocatalyst for pH-universal hydrogen evolution reaction and Zn-air batteries driven self-power water splitting. *J. Mater. Chem. A* **2023**, *11*, 18336–18348.
107. Zhang, Y.; Shi, W.; Bo, L.; et al. Electrospinning construction of heterostructural Co_3W_3C/CoP nanoparticles embedded in N, P-doped hierarchically porous carbon fibers as excellent multifunctional electrocatalyst for Zn-air batteries and water splitting. *Chem. Eng. J.* **2022**, *431*, 134188.
108. Luo, H.; Chen, X.; Huang, T.; et al. In situ simultaneously integrating Co-N-C sites and Co_9S_8 nanoparticles into N,S-doped porous carbon as trifunctional electrocatalysts for Zn–air batteries driving water splitting. *J. Environ. Chem. Eng.* **2022**, *10*, 107203.
109. Xin, R.; Zhao, H.; Liu, Y.; et al. Homologous Mott-Schottky electrocatalysts enable record cycling stability in Zn-Air battery and water splitting. *Adv. Funct. Mater.* **2025**, *36*, e24205.
110. Duan, X.; Pan, N.; Sun, C.; et al. MOF-derived Co-MOF, O-doped carbon as trifunctional electrocatalysts to enable highly efficient Zn-air batteries and water-splitting. *J. Energy Chem.* **2021**, *56*, 290–298. https://doi.org/10.1016/j.jechem.2020.08.007.
111. Liu, Q.; Shi, Q.; Ma, Y.; et al. ZIF-derived two-dimensional Co@carbon hybrid, toward highly efficient trifunctional electrocatalysts. *Chem. Eng. J.* **2021**, *423*, 130313.
112. Wang, F.; Xiao, Z.; Liu, X.; et al. Strategic design of cellulose nanofibers@ zeolitic imidazolate frameworks derived mesoporous carbon-supported nanoscale $CoFe_2O_4$/CoFe hybrid composition as trifunctional electrocatalyst for Zn-air battery and self-powered overall water-splitting. *J. Power Sources* **2022**, *521*, 230925. https://doi.org/10.1016/j.jpowsour.2021.230925.
113. Li, Y.; Liu, Y.; Qian, Q.; et al. Supramolecular assisted one-pot synthesis of donut-shaped CoP@PNC hybrid nanostructures as multifunctional electrocatalysts for rechargeable Zn-air batteries and self-powered hydrogen production. *Energy Storage Mater.* **2020**, *28*, 27–36. https://doi.org/10.1016/j.ensm.2020.02.022.
114. Sun, H.; Li, Q.; Lian, Y.; et al. Highly efficient water splitting driven by zinc-air batteries with a single catalyst incorporating rich active species. *Appl. Catal. B Environ.* **2020**, *263*, 118139. https://doi.org/10.1016/j.apcatb.2019.118139.
115. Han, S.; Chen, Y.; Hao, Y.; et al. Multi-dimensional hierarchical CoS_2@ MXene as trifunctional electrocatalysts for zinc-air batteries and overall water splitting. *Sci. China Mater.* **2021**, *64*, 1127–1138. https://doi.org/10.1007/s40843-020-1524-5.
116. Wang, S.; Wang, J.; Wang, X.; et al. Carbon hybrid with 3D nano-forest architecture in-situ catalytically constructed by CoFe alloy as advanced multifunctional electrocatalysts for Zn-air batteries-driven water splitting. *J. Energy Chem.* **2021**, *53*, 422–432. https://doi.org/10.1016/j.jechem.2020.07.045.
117. Li, J.; Tan, T.; Xie, Y.; et al. Bimetal-MOF and bacterial cellulose-derived three-dimensional N-doped carbon sheets loaded Co/CoFe nanoparticles wrapped graphite carbon supported on porous carbon nanofibers, An efficient multifunctional electrocatalyst for Zn-air batteries and overall water splitting. *J. Colloid. Interface Sci.* **2023**, *640*, 78–90. https://doi.org/10.1016/j.jcis.2023.02.058.
118. Wang, B.; Tang, C.; Wang, H.F. Anion-regulated hydroxysulfide monoliths as OER/ORR/HER electrocatalysts and their applications in self-powered electrochemical water splitting. *Small Methods* **2018**, *2*, 1800055.
119. Yan, L.; Xu, Z.; Liu, X.; et al. Integrating trifunctional Co@ NC-CNTs@ NiFe-LDH electrocatalysts with arrays of porous triangle carbon plates for high-power-density rechargeable Zn-air batteries and self-powered water splitting. *Chem. Eng. J.* **2022**, *446*, 137049.
120. Han, X.; Li, N.; Kang, Y.B.; et al. Unveiling trifunctional active sites of a heteronanosheet electrocatalyst for integrated cascade battery/electrolyzer systems. *ACS Energy Lett.* **2021**, *6*, 2460–2468. https://doi.org/10.1021/acsenergylett.1c00936.
121. Jian, J.; Zhang, Y.; Wang, Z.; et al. One-step synthesized iron foam-based $NiFe_2O_4$ applied for self-powered water splitting hydrogen production. *J. Mater. Chem. A* **2025**, *13*, 1102–1108.
122. Guo, W.; Luan, X.; Sun, P.; et al. A porous carbon layer wrapped Co_3Fe_7 alloy derived from a bimetallic conjugated microporous polymer as a trifunctional electrocatalyst for rechargeable Zn-air batteries and self-powered overall water splitting. *Sustainable Energy Fuels* **2021**, *5*, 6085–6096. https://doi.org/10.1039/d1se01225h.
123. Muthurasu, A.; Tiwari, A.P.; Chhetri, K.; et al. Construction of iron doped cobalt- vanadate- cobalt oxide with metal-organic framework oriented nanoflakes for portable rechargeable zinc-air batteries powered total water splitting. *Nano Energy* **2021**, *88*, 106238. https://doi.org/10.1016/j.nanoen.2021.106238.

124. Logeshwaran, N.; Ramakrishnan, S.; Chandrasekaran, S.S.; et al. An efficient and durable trifunctional electrocatalyst for zinc-air batteries driven overall water splitting. *Appl. Catal. B Environ.* **2021**, *297*, 120405. https://doi.org/10.1016/j.apcatb.2021.120405.
125. Ren, J.T.; Wang, Y.S.; Chen, L.; et al. Binary FeNi phosphides dispersed on N, P-doped carbon nanosheets for highly efficient overall water splitting and rechargeable Zn-air batteries. *Chem. Eng. J.* **2020**, *389*, 124408.
126. Liu, H.; Guan, J.; Yang, S.; et al. Metal-organic-framework-derived Co2P nanoparticle/multi-doped porous carbon as a trifunctional electrocatalyst. *Adv. Mater.* **2020**, *32*, 2003649. https://doi.org/10.1002/adma.202003649.
127. Liu, J.; Wang, C.; Sun, H.; et al. CoOx/CoNy nanoparticles encapsulated carbon-nitride nanosheets as an efficiently trifunctional electrocatalyst for overall water splitting and Zn-air battery. *Appl. Catal. B Environ.* **2020**, *279*, 119407. https://doi.org/10.1016/j.apcatb.2020.119407.
128. Ding, K.; Hu, J.; Jin, W.; et al. Dianion induced electron delocalization of trifunctional electrocatalysts for rechargeable Zn-air batteries and self-powered water splitting. *Adv. Funct. Mater.* **2022**, *32*, 2201944. https://doi.org/10.1002/adfm.202201944.
129. Yang, J.; Wang, X.; Li, B.; et al. Novel iron/cobalt-containing polypyrrole hydrogel-derived trifunctional electrocatalyst for self-powered overall water splitting. *Adv. Funct. Mater.* **2017**, *27*, 1606497. https://doi.org/10.1002/adfm.201606497.
130. Bai, Z.; Li, S.; Fu, J.; et al. Metal-organic framework-derived nickel cobalt oxysulfide nanocages as trifunctional electrocatalysts for high efficiency power to hydrogen. *Nano Energy* **2019**, *58*, 680–686. https://doi.org/10.1016/j.nanoen.2019.01.050.
131. Elhousseini Hilal, M.; Younus, H.A.; Chaemchuen, S.; et al. Sacrificial ZnO nanorods drive N and O dual-doped carbon towards trifunctional electrocatalysts for Zn-air batteries and self-powered water splitting devices. *Catal. Sci. Technol.* **2021**, *11*, 4149–4161. https://doi.org/10.1039/d1cy00119a.
132. Lv, X.W.; Xu, W.S.; Tian, W.W.; et al. Activity promotion of core and shell in multifunctional core-shell Co_2P@ NC electrocatalyst by secondary metal doping for water electrolysis and Zn-air batteries. *Small* **2021**, *17*, 2101856. https://doi.org/10.1002/smll.202101856.
133. Liu, P.; Gao, D.; Xiao, W.; et al. Self-powered water-splitting devices by core-shell NiFe@ N-graphite-based Zn–air batteries. *Adv. Funct. Mater.* **2018**, *28*, 1706928. https://doi.org/10.1002/adfm.201706928.
134. Liu, X.; Yin, Z.; Cui, M.; et al. Double shelled hollow CoS2@MoS2@NiS2 polyhedron as advanced trifunctional electrocatalyst for zinc-air battery and self-powered overall water splitting. *J. Colloid. Interface Sci.* **2022**, *610*, 653–662. https://doi.org/10.1016/j.jcis.2021.11.115.
135. Yao, J.; Wang, J.; Wang, W.; et al. Precision-engineered electronic modulation of ruthenium clusters and single atoms on vacancy-rich α-MoC1-x enables efficient electrocatalytic water splitting. *Adv. Mater.* **2026**, *38*, e19840.
136. Xu, Y.; Lv, H.; Lu, H.; et al. Mg/seawater batteries driven self-powered direct seawater electrolysis systems for hydrogen production. *Nano Energy* **2022**, *98*, 107295. https://doi.org/10.1016/j.nanoen.2022.107295.
137. Chen, C.; Fu, Z.; Qi, F.; et al. Fe^{2+}/Fe^{3+} cycling for coupling self-powered hydrogen evolution and preparation of electrode catalysts. *Angew. Chem. Int. Ed.* **2022**, *61*, 202207226.
138. Zhai, Y.; Jin, C.; Xia, Q.; et al. Atomically confined Ru sites in octahedral Co_3O_4 for high-efficiency hydrazine oxidation. *Adv. Funct. Mater.* **2024**, *34*, 2311063. https://doi.org/10.1002/adfm.202311063.
139. Peng, X.; Mi, Y.; Liu, X.; et al. Self-driven dual hydrogen production system based on a bifunctional single-atomic Rh catalyst. *J. Mater. Chem. A* **2022**, *10*, 6134–6145.
140. Li, Y.; Niu, S.; Liu, P.; et al. Ruthenium nanoclusters and single atoms on α-MoC/N-doped carbon achieves low-input/input-free hydrogen evolution via decoupled/coupled hydrazine oxidation. *Angew. Chem.* **2024**, *136*, 202316755. https://doi.org/10.1002/ange.202316755.
141. Sundar Rajan, A.P.; Senthil, R.A.; Moon, C.J.; et al. Self-powered hydrogen production via laser-coordinated NiCoPt alloy catalysts in an integrated Zn-hydrazine battery with hydrazine splitting. *Small Methods* **2025**, *9*, 2401709. https://doi.org/10.1002/smtd.202401709.
142. Yang, H.M.; Wang, H.Y.; Zhai, S.; et al. Aluminum-induced electron structure on nickel phosphide for effective hydrazine-assisted water splitting at large current density. *Chem. Eng. J.* **2024**, *489*, 151236.
143. Wang, H.Y.; Wang, L.; Ren, J.T.; et al. Taking advantage of potential coincidence region, advanced self-activated/propelled hydrazine-assisted alkaline seawater electrolysis and Zn–hydrazine battery. *ACS Nano* **2023**, *17*, 10965–10975. https://doi.org/10.1021/acsnano.3c03095.
144. Wang, J.; Guan, X.; Li, H.; et al. Robust Ru-N metal-support interaction to promote self-powered H_2 production assisted by hydrazine oxidation. *Nano Energy* **2022**, *100*, 107467. https://doi.org/10.1016/j.nanoen.2022.107467.
145. Wang, H.Y.; Wang, L.; Ren, J.T.; et al. Heteroatom-induced accelerated kinetics on nickel selenide for highly efficient hydrazine-assisted water splitting and Zn-hydrazine battery. *Nano-Micro Lett.* **2023**, *15*, 155. https://doi.org/10.1007/s40820-023-01128-z.

146. Zhao, X.; Zheng, H.; Sun, H.; et al. Restructuring hydrogen bond networks and enhancing dehydrogenation kinetics for efficient hydrazine oxidation-assisted electrolytic hydrogen production. *Adv. Energy Mater.* **2026**, *16*, 04983. https://doi.org/10.1002/aenm.202504983.
147. Yu, Q.; Liu, X.; Liu, G.; et al. Constructing three-phase heterojunction with 1D/3D hierarchical structure as efficient trifunctional electrocatalyst in alkaline seawater. *Adv. Funct. Mater.* **2022**, *32*, 2205767. https://doi.org/10.1002/adfm.202205767.
148. Meng, Y.; Xiang, C.; Zhang, W.; et al. Heteroatom-engineering promoted Co_9S_8 Bi-functional electrocatalyst for hydrazine-assisted hydrogen production at industrial current density. *Adv. Funct. Mater.* **2025**, *36*, e24807.
149. Shi, H.; Dai, T.Y.; Sun, X.Y.; et al. High-entropy alloy/intermetallic compound heterostructures for efficient hydrazine oxidation-assisted hydrogen production. *Adv. Mater.* **2025**, *37*, e12081. https://doi.org/10.1002/adma.202512081.
150. Wang, H.Y.; Yan, F.; Wang, H.; et al. The combination of electronic structure and lattice strain engineering for multi-powered hydrazine-assisted seawater electrolysis system at high current densities. *Adv. Energy Mater.* **2024**, *14*, 2402611. https://doi.org/10.1002/aenm.202402611.
151. Guan, X.; Sun, Y.; Zhao, S.; et al. Selectively nucleotide-derived RuP on N,P-codoped carbon with engineered mesopores for energy-efficient hydrogen production assisted by hydrazine oxidation. *SusMat* **2024**, *4*, 166–177. https://doi.org/10.1002/sus2.186.
152. Huang, J.; Jin, M.; Zhang, H.; et al. Manipulating the d-band center of Ir by metal-support interaction to optimize the adsorption for self-powered hydrazine oxidation-assisted hydrogen generation. *Energy Environ. Mater.* **2026**, *9*, e70159.
153. Ji, K.; Wang, S.; Yao, S.; et al. Modeling carbon-free energy conversion systems, enhanced hydrazine-assisted hydrogen production with dual-electric-field effect on needle-like Ru/CoP catalysts. *Energy Environ. Sci.* **2025**, *18*, 4764–4774. https://doi.org/10.1039/d4ee05691d.
154. Yu, Z.; D'Olimpio, G.; Huang, H.; et al. Self-powered hydrogen production from seawater enabled by trifunctional exfoliated PtTe nanosheet catalysts. *Adv. Funct. Mater.* **2024**, *34*, 2403099. https://doi.org/10.1002/adfm.202403099.
155. Guan, X.; Wu, Q.; Li, H.; et al. Identifying the roles of Ru single atoms and nanoclusters for energy-efficient hydrogen production assisted by electrocatalytic hydrazine oxidation. *Appl. Catal. B Environ.* **2023**, *323*, 122145. https://doi.org/10.1016/j.apcatb.2022.122145.
156. Hu, Y.; Chao, T.; Li, Y.; et al. Cooperative Ni(Co)-Ru-P sites activate dehydrogenation for hydrazine oxidation assisting self-powered H_2 production. *Angew. Chem. Int. Ed.* **2023**, *62*, 202308800.
157. Zhang, L.; Li, M.; Sun, C.; et al. A Hydrazine-water galvanic cell-inspired self-powered high-rate hydrogen production via overall hydrazine electrosplitting. *Adv. Funct. Mater.* **2025**, *35*, 2420163. https://doi.org/10.1002/adfm.202420163.
158. Zhao, S.; Zhang, Y.; Li, H.; et al. Regulating Ru active sites by Pd alloying to significantly enhance hydrazine oxidation for energy-saving hydrogen production. *J. Mater. Chem. A* **2023**, *11*, 13783–13792.
159. Zhai, X.; Yu, Q.; Chi, J.; et al. Accelerated dehydrogenation kinetics through Ru, Fe dual-doped Ni_2P as bifunctional electrocatalyst for hydrazine-assisted self-powered hydrogen generation. *Nano Energy* **2023**, *105*, 108008. https://doi.org/10.1016/j.nanoen.2022.108008.
160. Luo, J.; Yang, R.; Ma, Y.; et al. Interfacial Disorder platinum boosts trifunctional performance for hydrazine-assisted self-driven hydrogen generation. *Adv. Funct. Mater.* **2025**, *35*, 2503066. https://doi.org/10.1002/adfm.202503066.
161. Li, Y.; Zhang, J.; Liu, Y.; et al. Partially exposed RuP_2 surface in hybrid structure endows its bifunctionality for hydrazine oxidation and hydrogen evolution catalysis. *Sci. Adv.* **2020**, *6*, 4197.
162. Wang, G.; Chen, J.; Cai, P.; et al. A self-supported Ni-Co perselenide nanorod array as a high-activity bifunctional electrode for a hydrogen-producing hydrazine fuel cell. *J. Mater. Chem. A* **2018**, *6*, 17763–17770.
163. Quan, Q.; Li, X.; Song, C.; et al. Polyoxometalate-derived bi-functional crystalline/amorphous interfaces with optimized d-electron configuration for efficient self-powered hydrazine-seawater splitting. *Chem. Eng. J.* **2024**, *488*, 150897.
164. Sun, F.; Qin, J.; Wang, Z.; et al. Energy-saving hydrogen production by chlorine-free hybrid seawater splitting coupling hydrazine degradation. *Nat. Commun.* **2021**, *12*, 4182. https://doi.org/10.1038/s41467-021-24529-3.
165. Liu, Y.; Zhang, J.; Li, Y.; et al. Realizing the synergy of interface engineering and chemical substitution for Ni_3N enables its bifunctionality toward hydrazine oxidation assisted energy-saving hydrogen production. *Adv. Funct. Mater.* **2021**, *31*, 2103673. https://doi.org/10.1002/adfm.202103673.
166. Qian, Q.; Zhang, J.; Li, J.; et al. Artificial heterointerfaces achieve delicate reaction kinetics towards hydrogen evolution and hydrazine oxidation catalysis. *Angew. Chem.* **2021**, *133*, 6049–6058. https://doi.org/10.1002/ange.202014362.
167. Liu, X.; He, J.; Zhao, S.; et al. Self-powered H_2 production with bifunctional hydrazine as sole consumable. *Nat. Commun.* **2018**, *9*, 4365. https://doi.org/10.1038/s41467-018-06815-9.
168. Liu, Y.; Zhang, J.; Li, Y.; et al. Manipulating dehydrogenation kinetics through dual-doping Co_3N electrode enables highly efficient hydrazine oxidation assisting self-powered H_2 production. *Nat. Commun.* **2020**, *11*, 1853. https://doi.org/10.1038/s41467-020-15563-8.

169. Meng, G.; Chang, Z.; Zhu, L.; et al. Adsorption site regulations of [W-O]-doped CoP boosting the hydrazine oxidation-coupled hydrogen evolution at elevated current density. *Nano-Micro Lett.* **2023**, *15*, 212. https://doi.org/10.1007/s40820-023-01185-4.
170. Chi, J.; Guo, L.; Mao, J.; et al. Modulation of electron structure and dehydrogenation kinetics of nickel phosphide for hydrazine-assisted self-powered hydrogen production in seawater. *Adv. Funct. Mater.* **2023**, *33*, 2300625. https://doi.org/10.1002/adfm.202300625.
171. Zhu, L.; Huang, J.; Meng, G.; et al. Active site recovery and NN bond breakage during hydrazine oxidation boosting the electrochemical hydrogen production. *Nat. Commun.* **2023**, *14*, 1997. https://doi.org/10.1038/s41467-023-37618-2.
172. Liu, F.; He, L.; Ji, L.; et al. Bipolar hydrogen production from a hybrid alkaline-acidic formaldehyde-proton fuel cell. *Adv. Sci.* **2026**, *13*, e22899.
173. Liu, S.Q.; Xie, S.; Wu, S.; et al. Self-powered system for H2 production and biomass upgrading. *Adv. Funct. Mater.* **2024**, *34*, 2404105. https://doi.org/10.1002/adfm.202404105.
174. Wang, P.; Chen, K.; Chen, J.; et al. Trifunctional intermetallic PtZn-based electrocatalyst for integrated hybrid acid/alkali electrochemical cell toward glycerol conversion and H2 generation. *Adv. Funct. Mater.* **2024**, *34*, 2408267. https://doi.org/10.1002/adfm.202408267.
175. Zhu, W.; Zhang, X.; Yao, F.; et al. A hydrazine-nitrate flow battery catalyzed by a bimetallic RuCo Precatalyst for wastewater purification along with simultaneous generation of ammonia and electricity. *Angew. Chem. Int. Ed.* **2023**, *62*, 202300390.
176. Wang, B.; Xiao, X.; Li, J.; et al. Sulfion oxidation assisting self-powered hydrogen production system based on efficient catalysts from spent lithium-ion batteries. *Proc. Natl. Acad. Sci. USA* **2023**, *120*, e2317174120.
177. Ren, J.T.; Chen, L.; Wang, L.; et al. Multifunctional metal-phosphide-based electrocatalysts for highly efficient solar hydrogen production integrated devices. *J. Mater. Chem. A* **2023**, *11*, 2899–2909.
178. Saha, S.; Kharwar, Y.P.; Ghorai, S.; et al. A Heterogenised molecular electrocatalyst for round-the-clock green hydrogen production by solar-electrolyser and zinc-air batteries. *Angew. Chem. Int. Ed.* **2025**, *64*, e202516482.
179. Zhong, Y.; Lu, Y.; Pan, Z.; et al. Efficient water splitting system enabled by multifunctional platinum-free electrocatalysts. *Adv. Funct. Mater.* **2021**, *31*, 2009853.
180. Son, H.J.; Kim, M.J.; Ahn, S.H. Monolithic Co-NC membrane integrating Co atoms and clusters as a self-supporting multi-functional electrode for solid-state zinc–air batteries and self-powered water splitting. *Chem. Eng. J.* **2021**, *414*, 128739.
181. Yang, X.; Zhou, Z.; Zou, Y.; et al. Interface reinforced 2D/2D heterostructure of Cu-Co oxides/FeCo hydroxides as monolithic multifunctional catalysts for rechargeable/flexible zinc-air batteries and self-powered water splitting. *Appl. Catal. B Environ.* **2023**, *325*, 122332.
182. Tian, W.W.; Ying, Y.D.; Ren, J.T.; et al. A trifunctional $Co_{0.85}Se$/NC collaborated electrocatalyst enables a self-powered energy system for uninterrupted H_2 production. *J. Mater. Chem. A* **2023**, *11*, 8024–8037.
183. Xiao, R.; Wang, F.; Luo, L.; et al. Efficient self-powered overall water splitting by Ni_4Mo/MoO_2 heterogeneous nanorods trifunctional electrocatalysts. *Small Methods* **2023**, *7*, 2201659.
184. Hao, X.; Che, X.; Zhuo, X.; et al. Synchronized sulfur resource recovery and hydrogen production via a self-powered system based on multifunctional Co_3S_4 catalyst. *Int. J. Hydrogen Energy* **2024**, *69*, 31–38.
185. Hao, X.; Jiang, K.; Liu, G.; et al. A multifunctional MoS_2/Ni_9S_8/NF catalyst for synchronous desulfurization and hydrogen evolution by a self-driven system. *J. Mater. Chem. A* **2024**, *12*, 23732–23742.
186. Gao, S.; Jin, M.; Sun, J.; et al. Coralloid Au enables high-performance Zn-CO_2 battery and self-driven CO production. *J. Mater. Chem. A* **2021**, *9*, 21024–21031.
187. Zhang, Y.; Wu, P.; Chen, C.; et al. Electrochemical power sources enabled by multi-ion carriers. *Chem. Soc. Rev.* **2025**, *54*, 9685–9806.
188. Zhong, X.; Shao, Y.; Chen, B.; et al. Rechargeable zinc–air batteries with an ultralarge discharge capacity per cycle and an ultralong cycle life. *Adv. Mater.* **2023**, *35*, 2301952.
189. Wu, S.; Chen, H.; Jia, C.; et al. Bifunctional electroreduction catalysts of NiFe alloy on N-doped carbon toward industrial-level CO_2 conversion powered by Zn–air batteries. *Inorg. Chem. Front.* **2023**, *10*, 4484–4495.
190. Gao, S.; Wang, T.; Jin, M.; et al. Bifunctional Nb-NC atomic catalyst for aqueous Zn-air battery driving CO_2 electrolysis. *Sci. China Mater.* **2023**, *66*, 1013–1023.
191. Zhu, J.; Zhang, Q.; Wang, C.; et al. Improved performances toward electrochemical carbon dioxide and oxygen reductions by iron-doped stannum nanoparticles. *Nanoscale* **2025**, *17*, 2709–2717.
192. Han, J.; Shi, L.; Xie, H.; et al. Self-Powered Electrochemical CO_2 Conversion Enabled by a Multifunctional Carbon-Based Electrocatalyst and a Rechargeable Zn–Air Battery. *Small* **2024**, *20*, 2401766.
193. Li, J.; Wen, Z.; Xu, Q.; et al. N-doped carbon networks as bifunctional electrocatalyst toward integrated electrochemical devices for Zn-air batteries driving microbial CO_2 electrolysis cell. *J. CO2 Util.* **2022**, *62*, 102068.

194. Guan, J.; Zhou, B.; Wang, S.; et al. Accelerating hydrogen transfer kinetics at atomical interfaces for self-powered ammonia generation coupled with hydrazine oxidation. *Adv. Funct. Mater.* **2026**, *36*, e25819.
195. Hu, H.; Pan, S.; Ma, Z.; et al. A self-powered system to electrochemically generate ammonia driven by palladium single atom electrocatalyst. *SusMat* **2024**, *4*, 237.
196. Gupta, D.; Kafle, A.; Mohanty, P.P.; et al. Self-powered NH_3 synthesis by trifunctional Co_2B-based high power density Zn–air batteries. *J. Mater. Chem. A* **2023**, *11*, 12223–12235.
197. Zhang, Q.; Qiu, S.; Wang, L.; et al. Multifunctional high-entropy alloys and oxides for self-powered electrocatalytic nitrate reduction to ammonia. *Chem. Eur. J.* **2025**, *31*, 202500887.
198. Xiao, T.; Jiang, J.; Liu, Q.; et al. Self-powered energy-efficient ammonia electrosynthesis via zinc-nitrite battery with bifunctional Pd-$Co(OH)_2$ electrocatalyst. *Mater. Today Phys.* **2025**, *58*, 101858.
199. Wang, X.; Ai, L.; Zeng, Q.; et al. Waste to treasure, Self-powered electrocatalytic upgrading of nitrite and PET plastic wastes into value-added ammonia and formic acid over core–shell Ru-Co_3O_4 heterojunctions. *Chem. Eng. J.* **2025**, *511*, 161855.
200. Zhang, C.; Wang, X.; Jiang, J.; et al. Self-powered energy-efficient electrochemical nitrite reduction coupled with sulfion oxidation for ammonia synthesis and sulfur recovery over hierarchical cobalt sulfide nanostructures. *Appl. Catal. B Environ. Energy* **2025**, *365*, 124991.
201. Wang, K.; Dai, Q.; Hu, C.; et al. Earth-abundant metal-free carbon-based electrocatalysts for Zn-air batteries to power electrochemical generation of H_2O_2 for in-situ wastewater treatment. *Chem. Eng. J.* **2021**, *416*, 128338.
202. Li, Y.; Ouyang, D.; Liu, X.; et al. Self-powered electrochemical synthesis of hydrogen peroxide from air and lignin. *Energy Environ. Sci.* **2025**, *18*, 3633–3646.